INVESTIGATION OF OPTIMUM LASER PUMPING

J. H. Jacob, et al.
Avco Everett Research Laboratory, Inc.
2385 Revere Beach Parkway
Everett MA 02149

November 1979
Final Technical Report for Period 15 August 1974 to 31 July 1979

Sponsored by
DEFENSE ADVANCED RESEARCH PROJECTS AGENCY
DARPA Order No. 3500 Amend. I

Monitored by
OFFICE OF NAVAL RESEARCH
DEPARTMENT OF THE NAVY
Arlington VA 2217

FOREWORD

Contract No.: N00014-75-C-0062

DARPA Order No.: 3500 Amendment 1

Short Title of Work: Investigation of Optimum Laser Pumping

Contractor: Avco Everett Research Laboratory, Inc.
Everett, Massachusetts 02149

Principal Investigator: J.H. Jacob
(617) 389-3000 Ext. 329

Scientific Officer: Director, Physics Program
Physical Sciences Division
Office of Naval Research
800 North Quincy Street
Arlington, Virginia 22217

Effective Date of Contract: 15 August 1974

Contract Expiration Date: 31 July 1979

Amount of Contract: $1,667,957

UNCLASSIFIED

SECURITY CLASSIFICATION OF THIS PAGE (When Data Entered)

REPORT DOCUMENTATION PAGE		READ INSTRUCTIONS BEFORE COMPLETING FORM
1. REPORT NUMBER	2. GOVT ACCESSION NO.	3. RECIPIENT'S CATALOG NUMBER
4. TITLE (and Subtitle) (6) INVESTIGATION OF OPTIMUM LASER PUMPING.		5. TYPE OF REPORT & PERIOD COVERED (9) Final Technical Report. 15 Aug [redacted] 74 – 31 Jul [redacted] 79
		6. PERFORMING ORG. REPORT NUMBER
7. AUTHOR(s) (10) J.H. Jacob, R. Brochu, A. Hawryluk, J. Hsia, M. Rokni, ~~R.N. Srivastava and D. Trainor~~		8. CONTRACT OR GRANT NUMBER(s) (15) N00014-75-C-0062, DARPA Order-3500
9. PERFORMING ORGANIZATION NAME AND ADDRESS Avco Everett Research Laboratory, Inc 2385 Revere Beach Parkway Everett, MA 02149		10. PROGRAM ELEMENT, PROJECT, TASK AREA & WORK UNIT NUMBERS (12) 95
11. CONTROLLING OFFICE NAME AND ADDRESS Defense Advanced Research Projects Agency DARPA Order No. 3500 Amendment 1		12. REPORT DATE (11) Nov [redacted] 79 13. NUMBER OF PAGES 89
14. MONITORING AGENCY NAME & ADDRESS (if different from Controlling Office) Office of Naval Research Department of the Navy Arlington, VA 22217		15. SECURITY CLASS. (of this report) Unclassified
		15a. DECLASSIFICATION/DOWNGRADING SCHEDULE

16. DISTRIBUTION STATEMENT (of this Report)

Approved for public release; distribution unlimited.

17. DISTRIBUTION STATEMENT (of the abstract entered in Block 20, if different from Report)

18. SUPPLEMENTARY NOTES

19. KEY WORDS (Continue on reverse side if necessary and identify by block number)

Visible Lasers
UV Lasers
Discharge Physics
Boltzmann Analysis

20. ABSTRACT (Continue on reverse side if necessary and identify by block number)

The objective of this program is to characterize the performance of various laser candidate systems so that reliable projections of their usefulness for long-range DARPA missions can be properly assessed. In this final report, we highlight the accomplishments attained under this contract and summarize those results obtained in the interium period since the last Semi-Annual Technical Report. These include: (1) an attachment rate constant determination for the reaction e + Cl_2, (2) kinetic quenching measurements and role of →over

DD FORM 1 JAN 73 1473 EDITION OF 1 NOV 65 IS OBSOLETE

UNCLASSIFIED 048 450 plus

SECURITY CLASSIFICATION OF THIS PAGE (When Data Entered)

the $B\bar{\Sigma}$ and $C\bar{\Sigma}$ states in XeF*, (3) some preliminary results on active medium absorption in XeF* laser mixtures, (4) the effect of the ground state population on the XeF laser performance; and (5) a detailed model of e-beam pumped KrF* laser.

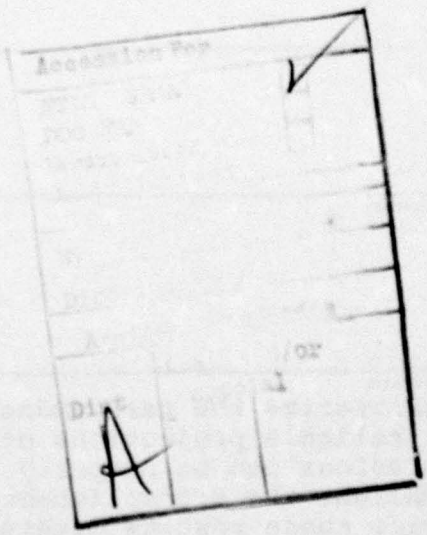

TABLE OF CONTENTS

LIST OF ILLUSTRATIONS

I. INTRODUCTION

This contract has made many contributions over the years to advance our understanding of the UV/visible laser candidates investigated as part of the DARPA/ONR program. For example, in FY75, we observed the first lasing by discharge pumping of a rare gas fluoride laser on the AERL small-scale apparatus.[1] Under this program a stability criterion for discharge pumping of electronic transition lasers was predicted theoretically and verified experimentally.[2] The formation efficiency of KrF* by discharge pumping was measured under stable discharge conditions and found to be 35%.[3] The gain and absorption in e-beam pumped KrF* and XeF* were also measured.[4,5] From these measurements, the dominant absorbing species were identified and we verified that self-absorption in KrF* was negligible. The above information, together with the AERL measured quenching kinetics, was incorporated into a kinetics/laser code. This code has successfully predicted the efficiency and laser flux extracted from the 1m, device.[6]

More recently, we have done preliminary experiments in discharge pumped mercury halides. For example, lasing of HgCl* by discharge pumping has been demonstrated.[7] In addition, a kinetic code has been written that includes the major reactions and the circuit equations. As in the earlier work on the discharge pumping of KrF*, we have included the effects of excited state excitation

and ionization. A stability theory that is applicable for metal vapor discharges has been completed.[8] This information has been summarized in earlier technical reports and open literature publications. More recently, in FY78, information on the extent of bottlenecking in XeF* was provided, temperature dependent rate constants for the dominant quenching processes involving XeF* were measured,[9] and experiments investigating the variation of absorption in XeF* active medium at elevated temperature were undertaken. These measurements also included the first direct measurement of the rate constant for electron quenching of XeF*.[9]

The information obtained in the program and the understanding of electronic transition lasers it represents has contributed significantly to the overall DARPA/ONR visible laser effort. Based on these key kinetic measurements and supporting laser experiments, we were able to project efficient, scalable operation of these laser candidates to meet a variety of DARPA mission objectives.

II. RESULTS

A. ELECTRON ATTACHMENT PROCESSES

Experiments performed under contract N00014-76-C-1032 demonstrated an intrinsic laser efficiency near 3% for e-beam-controlled discharge pumping of HgCℓ* in the one-meter laser device. One of the major technical issues for efficient laser operation is discharge stability which was discussed in considerable detail in an earlier report.[10] The discharge was shown to be stable if the following criterion was met for attachment dominated conditions:

$$\beta \geq m \nu_{i_o}$$

where $2 < m \leq 3$, ν_{i_o} is the equilibrium ionization rate and β is the attachment rate, i.e., $\beta = k_{ATT}[X]$ where k_{ATT} is the attachment rate constant and [X] denotes the density of attacher present.

Due to the importance of attachment in the successful modeling of the attachment dominated e-beam-controlled dishcarge lasers, we have hade a measurement of the rate constant for electron dissociative attachment to molecular chlorine used as a donor in the laser experiments. The halogen donor serves two basic functions: (1) it provides the halogen atom for the lasing exciplex; and (2) in helps stabilize the discharge by dissociatively attaching the secondary electrons.[7,2] For the HgCℓ* laser, $C\ell_2$ may be an

appropriate donor because it is known that the $Hg(^3P_2)$ level reacts with $C\ell_2$ to produce $HgC\ell^*$.[11] Before discharge pumping of $HgC\ell^*$ using $C\ell_2$ may be evaluated, the dissociative attachment rate of electrons by $C\ell_2$ has to be known.

Figure 1 shows the potential curves[12] of $C\ell_2$ and $C\ell_2^-$. From these curves it is apparent that there are three electron energies where the attachment cross section will have a maximum value corresponding to the transitions to the three non-bonding states. These peaks have been observed experimental by Tam and Wong[12] and Kurepa and Belic[13] who measured the shape of the attachment cross section as a function of electron energy for room temperature $C\ell_2$. Also, as the vibrational distribution of $C\ell_2$ changes, the attachment cross section and hence the attachment rate constant will change. Such a variation of attachment rate with vibrational temperature has been observed for other halogen compounds.[14] As the mercury monohalide lasers operate at 200-250°C, it is important to measure the attachment rate as a function of both electron temperature and gas temperature.

The experimental apparatus in which these measurements were made has been described previously.[1] The gas mixture was ionized by a beam of fast electrons having an energy of 150 keV and a current density of about 0.1 A/cm^2. About 40 ns after the e-beam was fired, a capacitor that was precharged to the relevant voltage was switched across the anode and cathode of the discharge cell. The discharge cell was constructed from stainless steel and could be heated to 250°C. The $C\ell_2$ density in the cell was monitored by

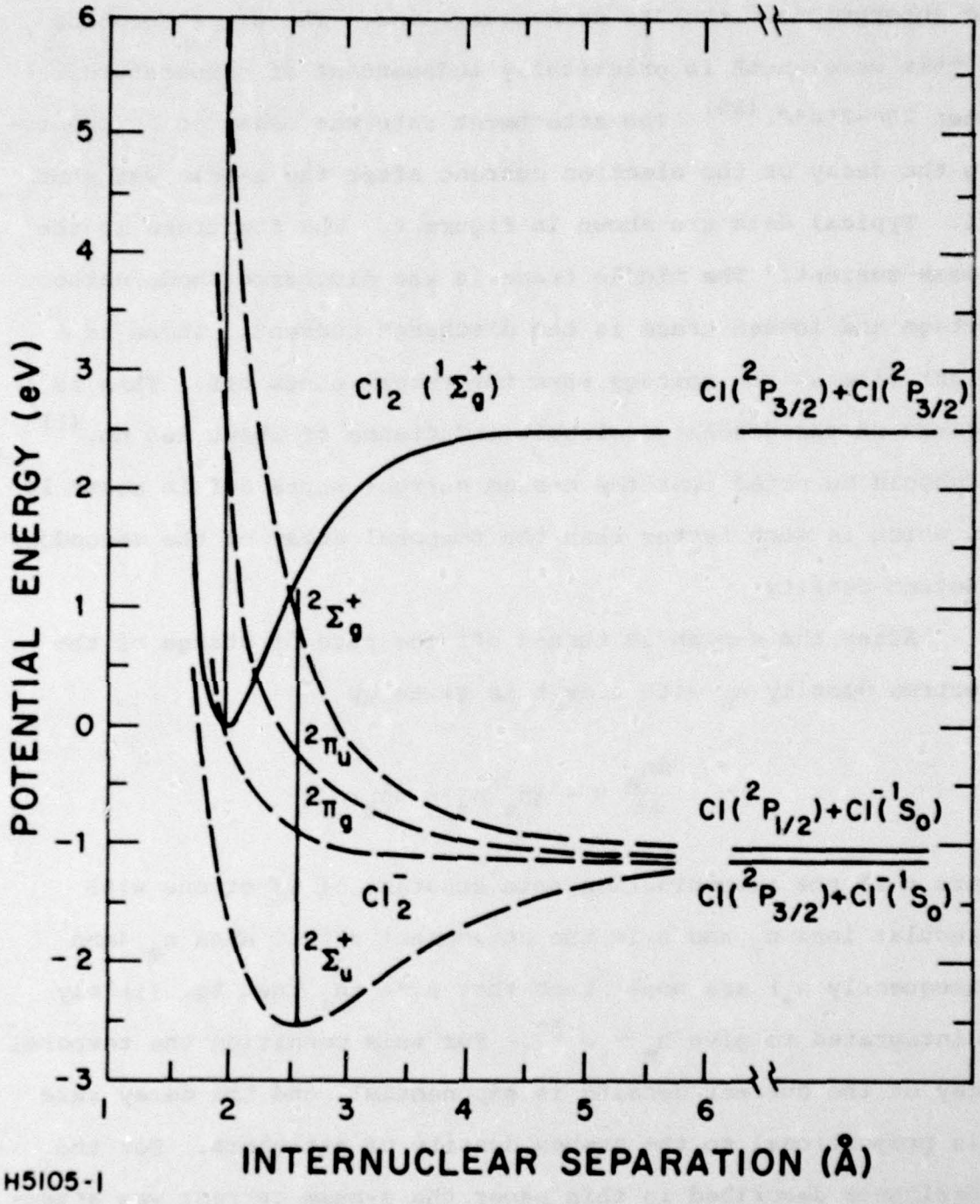

Figure 1 Potential Curves for $C\ell_2$ and $C\ell_2^-$

the absorption of the 366 nm mercury line. The $C\ell_2$ absorption at this wavelength is practically independent of temperature between 20°-250°C.[15] The attachment rate was measured by observing the decay of the electron current after the e-beam was shut off. Typical data are shown in Figure 2. The top trace is the e-beam current. The middle trace is the discharge anode/cathode voltage and lowest trace is the discharge current. There is a slight rise in the voltage when the e-beam shuts off. This is because of the discharge circuit inductance of about 160 nh.[1] It should be noted that the e-beam current shuts off in about 10 ns, which is much faster than the temporal decay of the secondary electron density.

After the e-beam is turned off the rate of change of the electron density n_e with time t is given by

$$\frac{dn_e}{dt} = - \alpha n_e n_+ - \beta n_e$$

where α is the recombination rate constant of electrons with molecular ions n_+ and β is the attachment rate. When n_e (and consequently n_+) are small such that $\beta >> \alpha n_+$ then Eq. (1) may be integrated to give $n_e \sim e^{-\beta t}$. For this condition the temporal decay of the current density is exponential, and the decay rate β is proportional to the number density of attachers. For the experiments described in this paper the e-beam current was attenuated to 0.1 A/cm^2 and $n_e \leq 3 \times 10^{13}$ cm^{-3}. Figure 3 shows the decay of the current on semi-log plots for mixtures containing

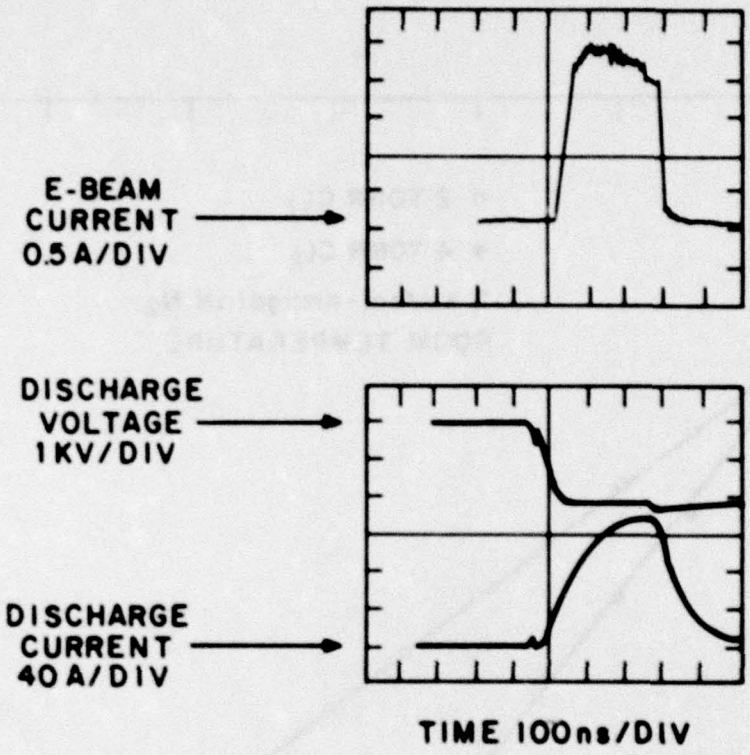

Figure 2 E-Beam Current, Discharge Voltage and Discharge Current Pulse Shapes

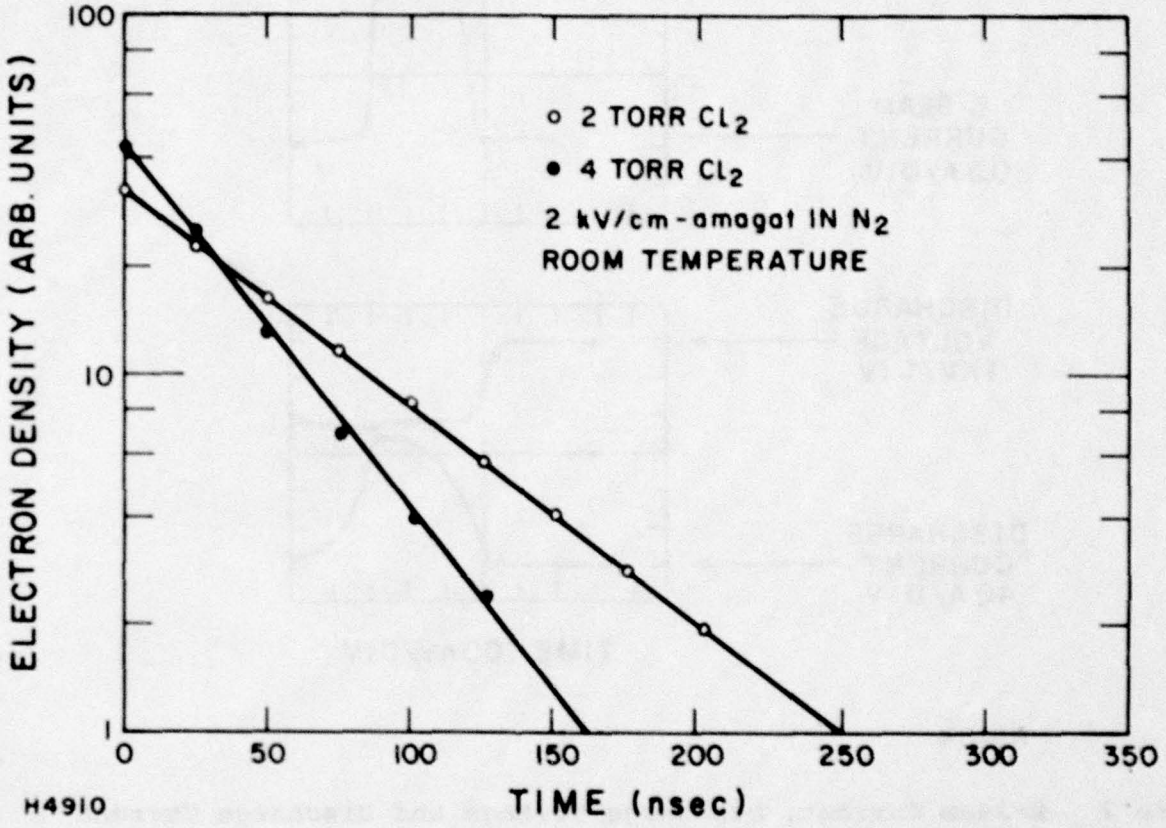

Figure 3 Semi-Log Plot of the Variation of n_e vs Time for N_2/Cl_2 Mixtures at Room Temperature

4 torr of $C\ell_2$ in one amagat of N_2. From this figure it is apparent that the decay is exponential for more than a decade of drop in n_e, verifying the the electron-ion recombination is negligible compared to the attachment rate. Moreover the attachment rate so measured is a linear function of the $C\ell_2$ density as shown in Figure 4. Experiments were performed at 2, 6 and 10 kV/cm-amagat. From the slope of these curves the attachment rate constant of $C\ell_2$ at a given electric field is determined. Figure 5 shows the results of similar experiments at 250°C. By comparing Figures 4 and 5 it is clear that the dissociative attachment rate in heated $C\ell_2$ is larger than that of room temperature $C\ell_2$. Figure 6 shows the results of the attachment rate constant for various E/N in N_2 mixtures for both room temperature and 250°C gas mixtures. In evaluating the E/N we have allowed for a cathode fall of 200 V. From the room temperature data we can calibrate the relative attachment cross section measured by Tam and Wong[12] and Kurepa and Belic.[13] The peak cross section near zero energy is 2.2×10^{-16} cm^2. Kurepa and Belic[13] estimated this peak value as 2×10^{-16} cm^2. For comparison, in Figure 6 we also show the variation of the attachment rate constant as predicted by the Boltzmann code[16] using Tam and Wong's cross section,[12] normalized by our measurements.

The attachment rate constant of $C\ell_2$ for thermal electrons at 300°K has been measured by Christodoulides, Schumacher and Schindler[17] to be 3.1×10^{-10} cm^3/s. Using our predicted peak

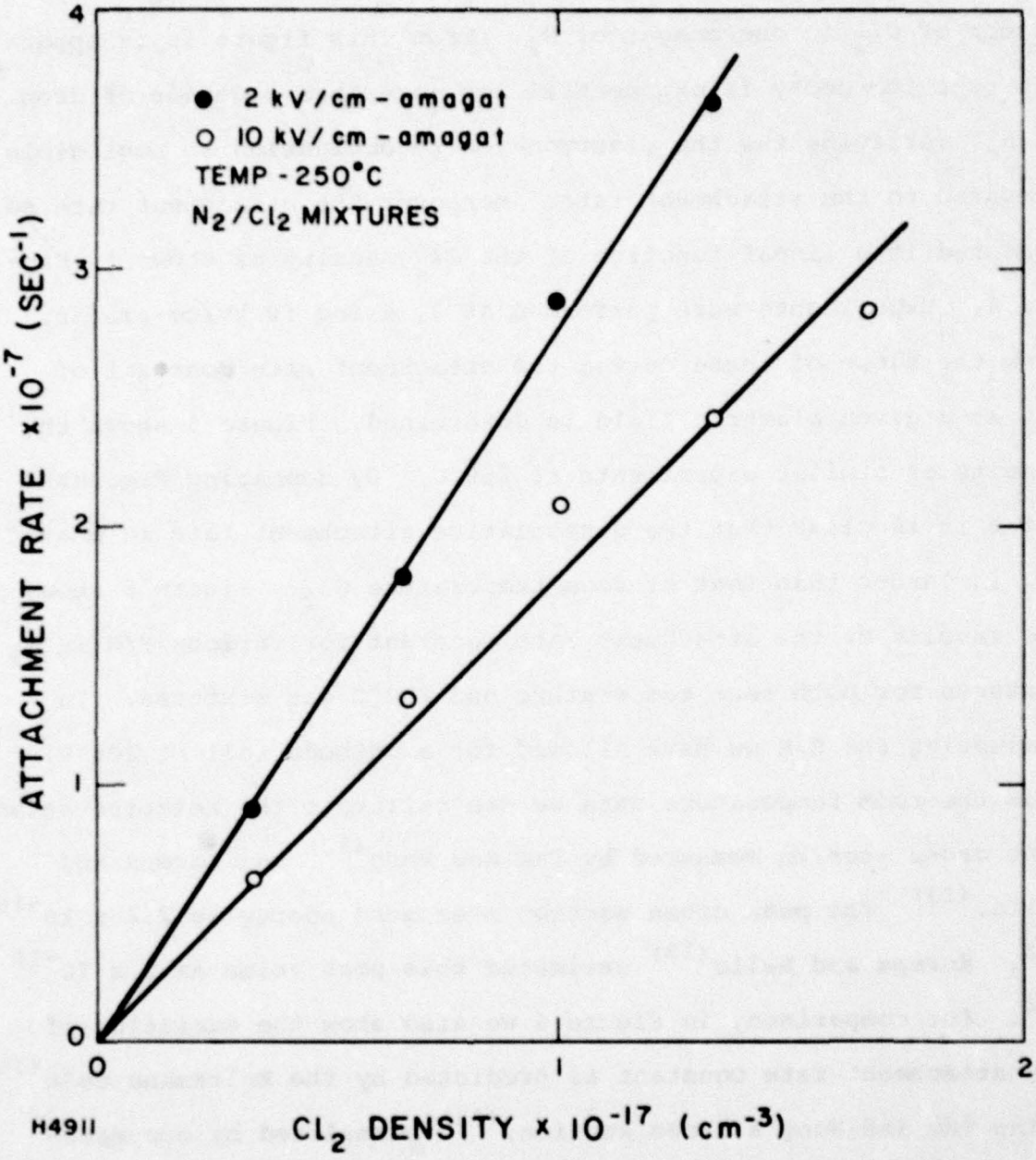

Figure 4 Attachment Rate as a Function of Cl_2 Density in N_2/Cl_2 Mixtures at Room Temperature

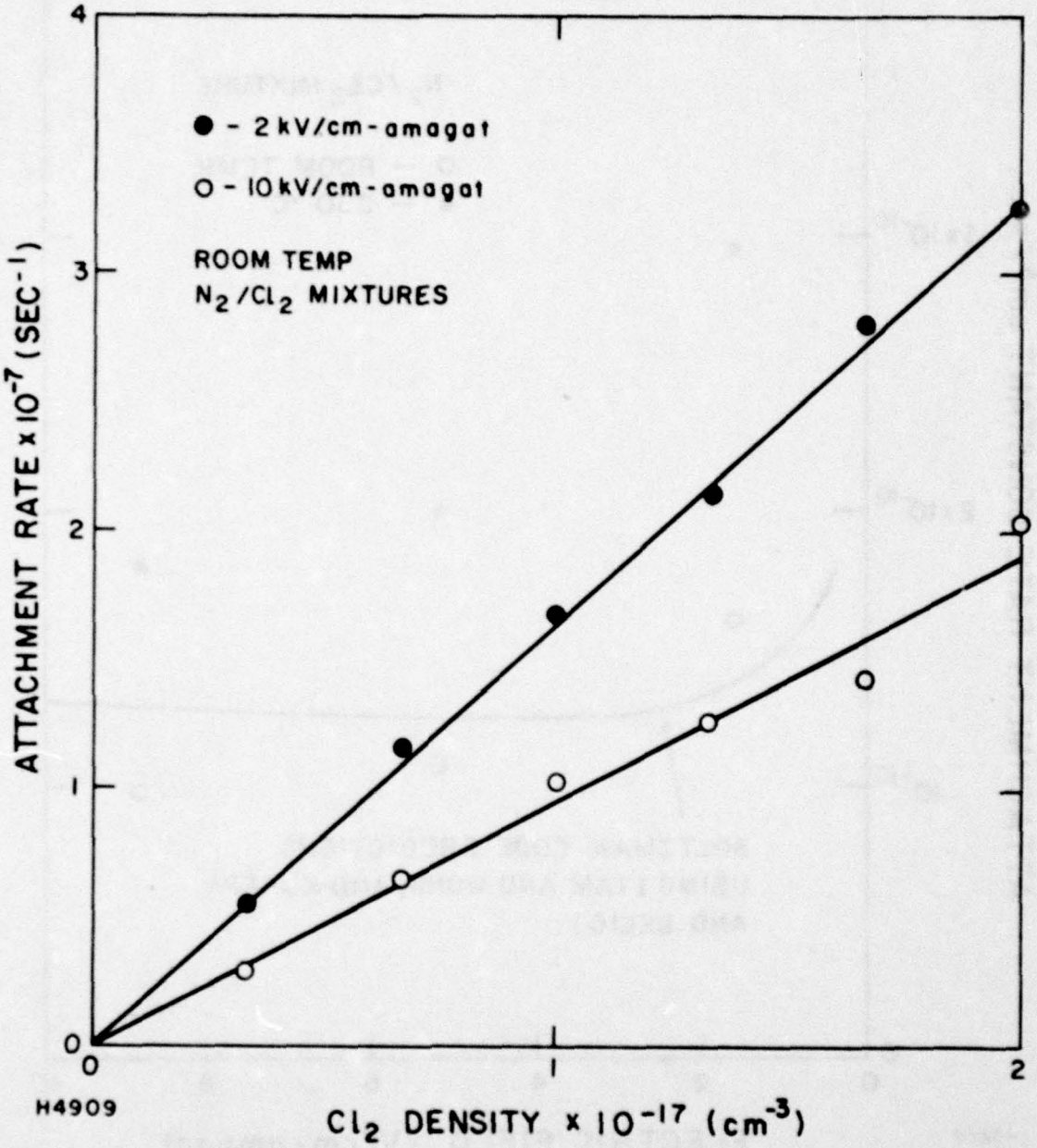

Figure 5 Attachment Rate as a Function of $C\ell_2$ Density in $N_2/C\ell_2$ Mixtures at 250°C

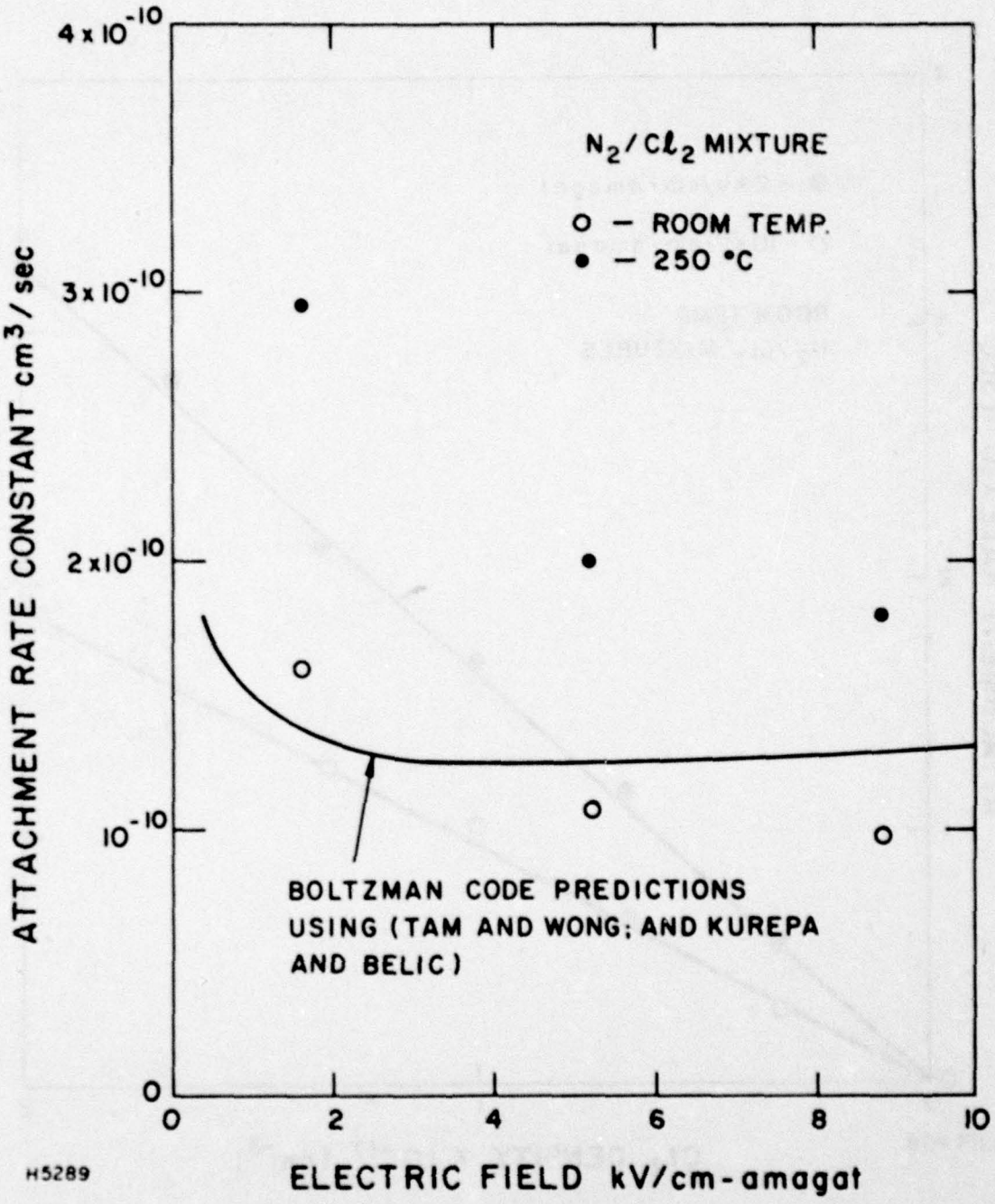

Figure 6 Attachment Rate Constant of Cl_2 at Room Temperature and 250°C. The solid curve is the predictions of the Boltzmann code for room temperature Cl_2.

value of 2.2×10^{-16} cm^2 we calculate that the rate constant for an electron temperature of 300°K should be $\approx 10^{-9}$ cm^3/s. This discrepancy, between the measurement of Christodoulides et al[17] and our calculation using the Tam and Wong's[12] cross section can be explained in part by the uncertainty of $\pm$ 0.05 eV in the electron energy. Also the e-beam used by Tam and Wong[12] had a width of ~ 0.05 eV causing an uncertainty in the width of the peak cross section near zero energy. Such an uncertainty is about 2 kT at room temperature and could greatly alter the estimated attachment rate constant for 300°K electrons.

Finally we have measured the attachment rate in $Ar/C\ell_2$ mixtures. The purpose for replacing the N_2 buffer with Ar is that in Ar the mean electron energy is considerably larger for the same E/N. For the Ar rich mixtures we ran at an electric field 2 kV/cm atm. The mean electron energy for this case was predicted to be 5.2 eV by the Boltzmann code. At room temperature the measured attachment rate constant was 2.04×10^{-10} cm^3/s. This value should be compared with the value of 3.3×10^{-10} cm^3/s predicted by the Boltzmann code using Tam and Wong's cross section,[12] and 2.9×10^{-10} cm^3/s, using Kurepa and Belic's cross section.[13] The attachment rate constant at 250°C in Ar was measured as 2.9×10^{-10} cm^3/s.

For the mercury monohalide e-beam-controlled laser discharges the electron energy will be determined largely by the mercury. The mean electron energy is approximately 1-2 eV.[18] The mixture temperature is approximately 250°C. So the measurements in the N_2 buffer gas discussed in the report will be applicable.

B. XeF* LASER KINETICS

The key physical processes governing the operation of e-beam excited XeF lasers are summarized in Figure 7. The e-beam deposits its energy in the laser gas mixture which results in the formation of XeF* exciplex states via a set of kinetic processes labeled "formation kinetics." An understanding of these processes is necessary in order to (1) choose the optimum gas mixture and excitation intensity, and (2) predict the formation efficiency and attainable specific pulse energy (J/l).

XeF* has two nearly energy-degenerate lowest ionic states. These are generally labeled XeF* (B) and XeF* (C). Since these states are close in energy, one expects substantial formation in both of these and, furthermore, once formed, they should also be coupled through collisions. Since generally lasing only occurs from the XeF*(B) state, one must consider the formation and the rate of collisional mixing between these states.

Once formed these XeF* states can spontaneously radiate, be quenched, or stimulated by the photon field. In order to calculate the cavity flux required to compete effectively against radiative and quenching processes, one must know the radiative lifetimes, the stimulated emission cross sections and the various quenching rate constants.

The lower laser level, the XeF*(X) ground state, is slightly bound ($\approx 1200\ cm^{-1}$)[19] and, therefore, for efficient laser operation it must be removed by volumetric processes. The rate with which this occurs determines the lower level density and extent of bottlenecking.

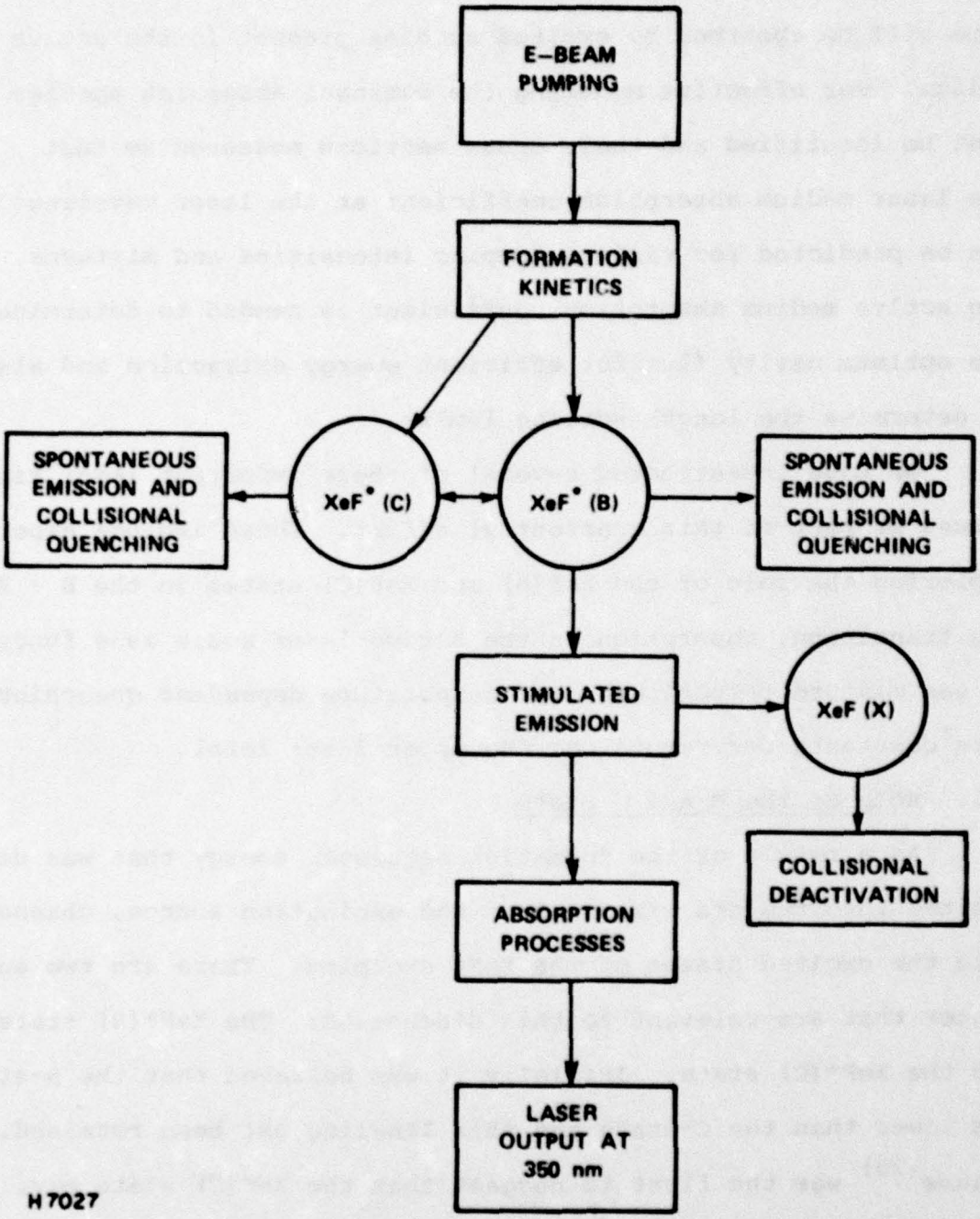

Figure 7 Key Issues in XeF Lasers

The stimulated photons must emerge from the laser cavity. Some will be absorbed by excited species present in the active medium. For effective modeling the dominant absorbing species must be identified and their cross sections measured so that the laser medium absorption coefficient at the laser wavelength can be predicted for various pumping intensities and mixtures. The active medium absorption coefficient is needed to determine the optimum cavity flux for efficient energy extraction and also to determine the length scaling limits.

We have investigated several of these important laser kinetic issues as part of this contractual effort. These include experiments exploring the role of the XeF(B) and XeF(C) states in the B → X lasing transition, absorption in the active laser media as a function of gas mixture temperature, and temperature dependent quenching rate constants for removal of the upper laser level.

1. Role of the B and C State

As a result of the formation sequence, energy that was deposited into the gas mixture from the excitation source, channels into the excited states of the XeF* exciplex. There are two such states that are relevant to this discussion: The XeF*(B) state and the XeF*(C) state. Initially it was believed that the B-state was lower than the C-state and this labeling has been retained. Krauss[20] was the first to suggest that the XeF(C) state may, in fact, be below the B-state and lie at greater internuclear separation. MOre recently, experiments performed by Setser, et al.[21] and Kligler, et al.[22] indicate that the C-state could be as much

as 0.08 eV below the B-state. This energy separation was deduced by observing the 350 nm and broadband fluorescence as a function of pressure. In this analysis it was assumed[21,22] that the broadband centered at 480 nm was solely due to C → A radiation. Julienne and Krauss[23] have recently shown that at the broadband wavelength there could also be a contribution from B → A radiation. However, taking this radiation into account, they find that reported separation[21,22] of the B- and C-states would change only slightly, (< 2%).

In this section, we report the results of our investigation regarding the relation between the narrowband and broadband emissions. In general our data suggest that: a) At low pressures the B- and C-states are not collisionally coupled and the formation from the ionic channel populates mainly the B-state. This lack of coupling at low pressures may have caused some of the disagreement among various kinetic rate constants, measured by different groups. b) The B- and C-states are well coupled at gas mixture pressures appropriate for laser action (> 1/2 atm) and under these conditions the energy stored in the C-state is amenable to the 350 nm laser transition. c) With increasing gas mixture pressure an extra contribution to the broadband appears, due to triatomic exciplexes (i.e., ArXeF*) formed by the three-body quenching of XeF*.

Two sets of experiments were performed. One set consisted of monitoring the absolute ratio of the 350 nm and the broadband intensities when the XeF* was produced by e-beam pumping, (pulselength ~ 300 ns, current denisty ~ 2 A/cm^2) and by short-pulse

excitation (pulse-length ~ 6 ns, 10 A/cm^2). Appropriate filters with two photodiodes were used for the simultaneous measurement of the two-band intensities. The filters were selected carefully so as to separate the two bands and to transmit the full energy content of the desired band. Assymetries in the experiment were corrected for by repeating the measurements when the filter sets were exchanged between the photodiodes.

The ratio of the narrow band intensity to the broadband intensity is plotted in Figure 8 as a function of gas mixture pressure for various inert gas/NF_3 mixtures. The NF_3 concentration was 0.2% for all mixtures and the Xe concentration in the mixtures with Ar or Ne as diluent was 2%. As seen in Figure 8, the intensity ratio decreases as the pressure rises until it approaches a constant asymptotic value near 1/2 atm. This asymptotic value is about 6-7 for Xe/NF_3 mixtures and decreases to 4-5 and 1-2 for Ne and Ar diluents, respectively. Similar results were obtained when these mixtures were excited by the 6 ns e-beam pulse. These results are very different from those reported by Setser et al.[21] and Kligler et al.[22] who observed an asymptotic value of about 0.3 for Ar, N_2 and He diluents.

The fact that the asympotatic value is dependent on the gas diluent used is a strong indication of the possibility of triatomic exciplexes' contribution to the emission at the broadband wavelength region. The possibility of triatomic exciplex contribution to the broadband is also compatible with the observed ordering of the asymptotic ratios (see Figure 8). For binary mixtures of

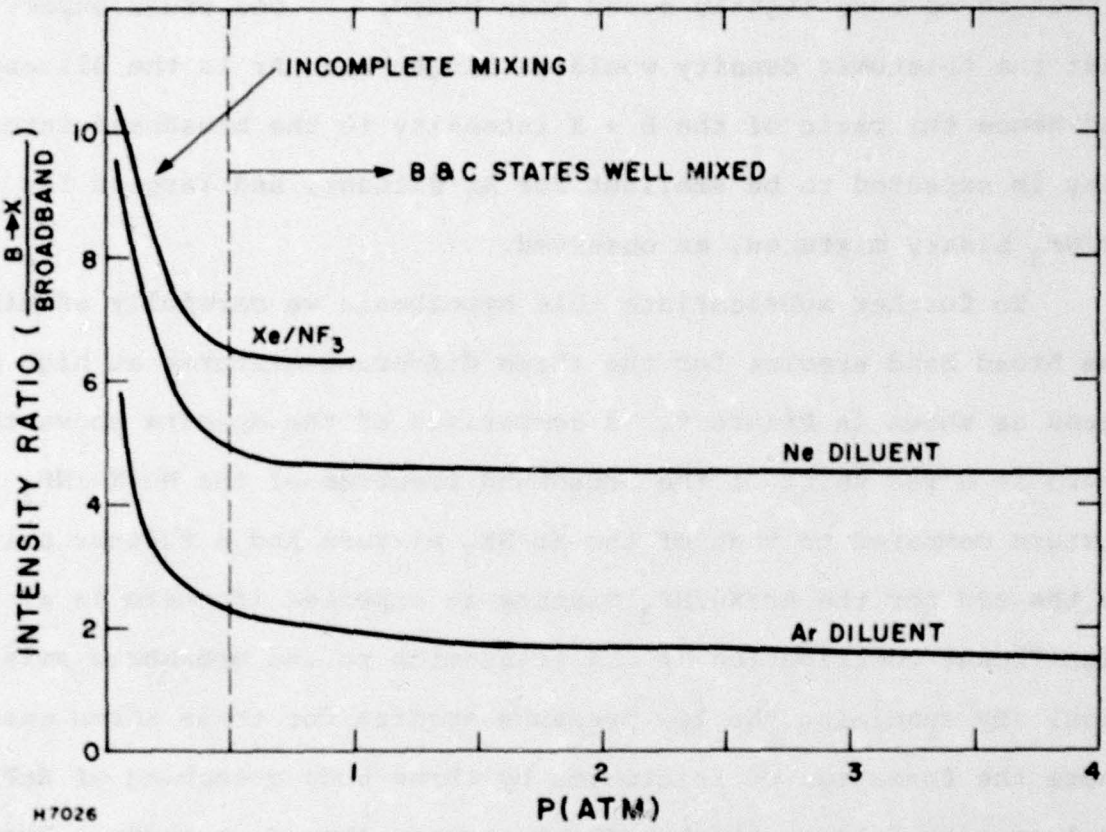

Figure 8 B → X to Broadband Intensity Ratio vs Pressure (The Curves are Averaged Over the Experimental Data)

Xe/NF_3, no triatomic emission should be observed near the broadband wavelength since the Xe_2F^* triatomic is expected to radiate at much longer wavelengths (> 1 μ). Also, since ArXeF* is predicted to be more tightly bound than NeXeF,[20] one would expect that the triatomic density would be larger when Ar is the diluent, and hence the ratio of the B → X intensity to the broadband intensity is expected to be smallest for Ar diluent, and largest for Xe/NF_3 binary mixtures, as observed.

To further substantiate this hypothesis we carefully examined the broad band spectra for the three different mixtures at high pressures as shown in Figure 9. A comparison of the spectra shows that there is a red shift of the broadband spectrum of the $Ne/Xe/NF_3$ mixture compared to that of the Xe/NF_3 mixture and a further shift to the red for the $Ar/Xe/NF_3$ mixture as expected if there is a significant contribution of the triatomics to the broadband emission. By examining the low pressure spectra for these three cases, where the formation of triatomics by three-body quenching of XeF* is less significant, the broadband spectra showed no shift. From these results we conclude that with Ar and Ne diluents there is a triatomic contribution to the broadband which becomes significant with increasing pressure.[24]

In addition to these fluorescence experiments, we have performed lasing experiments that show that the energy stored in the broadband is recoverable under B → X laser conditions. These experiments were performed by monitoring the sidelight fluorescence of the B → X transition and the broadband transition under lasing

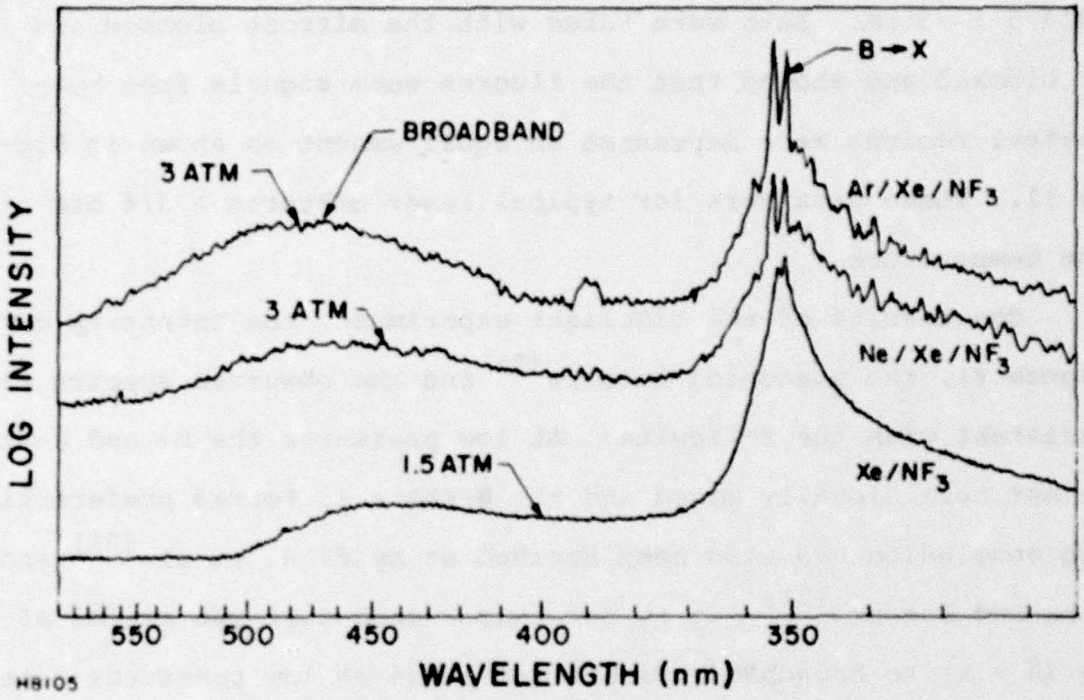

Figure 9 Spectra for B → X and Broadband Emission for Various Inert Gas/NF_3 Mixtures

and non-lasing conditions. The experimental apparatus is shown schematically in Figure 10 and has been described previously.[25] The active gain length was one meter and the mirrors were spaced 1.5 m apart. The spectral regions monitored are 350 ± 1.0 nm and 475 ± 75 nm. Data were taken with the mirrors blocked and not blocked and showed that the fluorescence signals from both spectral regions were depressed an equal amount as shown in Figure 11. These data were for typical laser mixtures > 3/4 atm at room temperature.

The results of the sidelight experiment, the intensity ratios (Figure 8), the quenching results[9] and the observed spectra are consistent with the following: At low pressures the B- and C-states are not collisionally mixed and the B-state is formed preferentially. This conclusion has also been arrived at by Finn, et al.[26] and Kolts and Setser.[21] It is for this reason that the ratios of the (B → X) to broadband emission is large at low pressures (see Figure 8). At high pressures the B- and C-states are well mixed by collisions and so can be considered as a single state. It is for this reason that the curves in Figure 8 for the Xe buffer reaches an asymptote (for these runs the "broadband" is presumed to be entirely C → A and B → A). From the asymptotic value of the intensity ratio for xenon, one can compute the B- to C-state energy spacing with out data as was done in Ref. 21 and 32. Using a spontaneous lifetime ratio of 9.3 for the C- and B-states, then the data suggests that the C-state lies below the B-state by

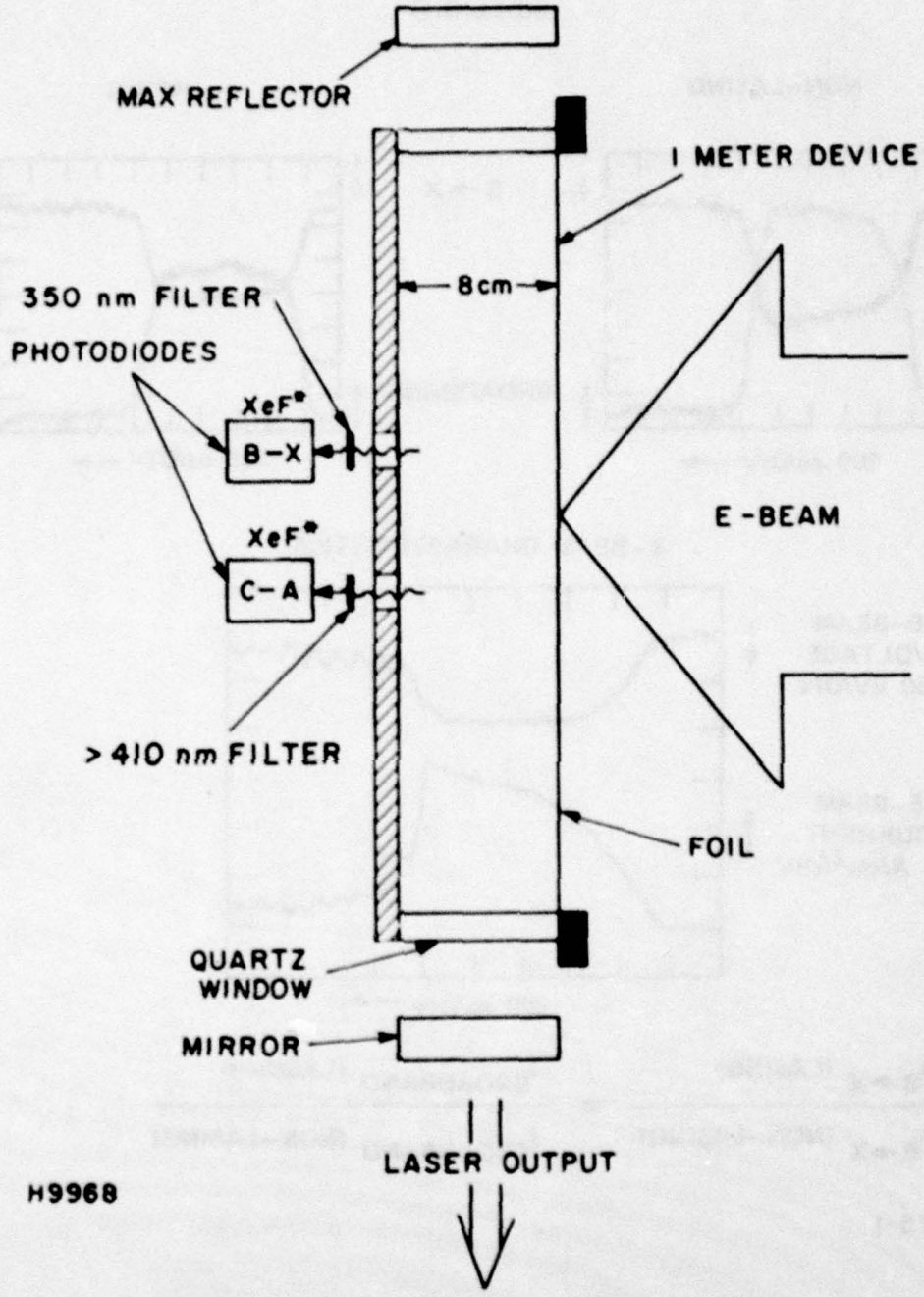

Figure 10 Schematic Showing Sidelight Fluorescence Measurements Under Lasing and Non-Lasing Conditions

(No DILUENT, 2 ATM)

SIDELIGHT

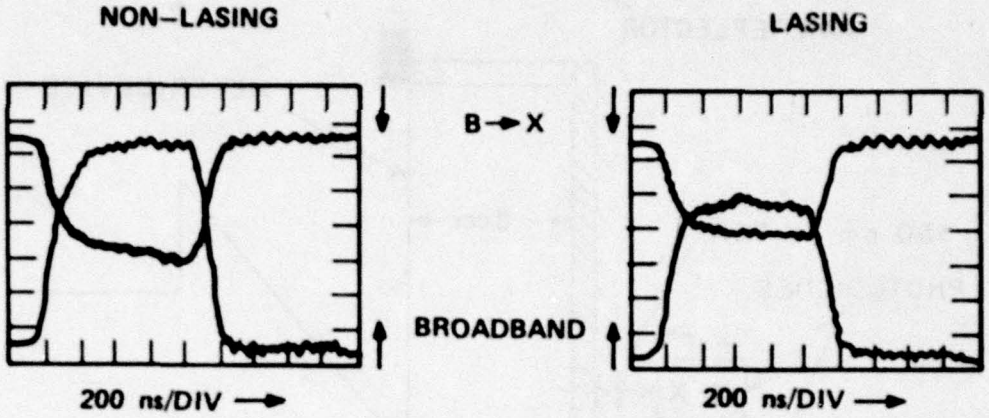

E–BEAM CHARACTERISTICS

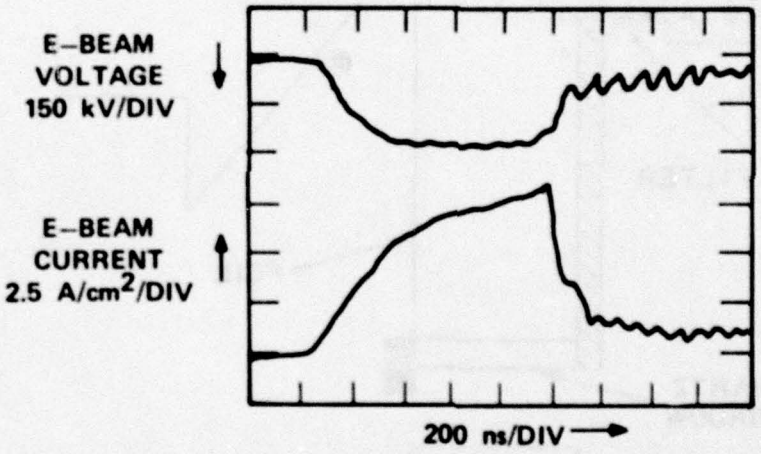

$$\frac{I_{B\rightarrow X}\ (\text{LASING})}{I_{B\rightarrow X}\ (\text{NON–LASING})} \approx \frac{I_{\text{BROADBAND}}\ (\text{LASING})}{I_{\text{BROADBAND}}\ (\text{NON–LASING})}$$

H7025-I

Figure 11 Data of the Sidelight Fluorescence for Lasing and Non-Lasing Conditions

$\approx kT/5$; where T is the temperature of the mixing agent. The mixing could be due to electrons[22] or heavy particles. It is unlikely that the electrons are mixing the B- and C-states for the following reasons. Under the present experimental conditions, the electron density for the data shown in Figure 8 is almost independent of pressure for a given mixture. So if electrons were responsible for mixing the B- C-states, one would expect the ratio of the intensities to be independent of pressure, which is clearly not the case. The conclusion that electrons are not the dominant mixing agent for the B- and C-states has also been arrived at by Finn, et al.[26] Hence, the mixing must be a result of heavy particles collisions. By substituting the ambient temperature (300°K), we find from these data that the C-state is lower than the B-state by $\lesssim 0.01$ eV, which is much smaller than the results of Setser, et al.[21] and Kligler, et al.[22]

Although our model is self-consistent, an alternative explanation is that XeF(B) is primarily formed and XeF(C) is subsequently formed by XeF(B) quenching processes.[26] Such a model would also explain the observed depression of the broadband under lasing conditions. However, in this model (using the published B-C quenching rate constants),[22,24] the XeF(B) fluorescence efficiency would be 60% smaller than we have previously measured.[6] Furthermore, this model cannot account for the measured three-body quenching of XeF(B) and the observed wavelength shift of the broadband emission in the various mixtures.

2. Absorption in the Active Laser Media

An additional competing process for efficient laser operation and one that may limit the length scaling of any operational laser device is the extent of the active media's absorption. AFRL had provided information on gain and absorption in KrF* laser mixes[27] and also neon and argon rich XeF* laser mixtures.[28] These results showed the importance of using neon as a diluent, since in neon-rich mixtures the formation of Xe_2^+ is significantly curtailed. This molecular ion has strong absorption at XeF* lasing wavelengths as seen in Figure 12. In neon-rich mixtures, Ne_2^+ is the principal dimer ion and, therefore, we were interested in the effect of temperature on the total absorption.

These experiments were carried out using a flashlamp pumped dye laser operating at 338 ± 2 nm with p-terphenyl as the solute (see Figure 13). This is essentially the same experimental set-up used for the room temperature measurements. We first verified the measurements at room temperature and then took additional data at 400° and 450°K (see Figure 14). These data indicated the absorption cross section at higher temperature seemed to lessen by about 40% at pressures near 2 amagat. This decrease in active media absorption has a positive effect on the laser performance and accounts for some of the increase in efficiency observed in the 1-m lasing experiments.

3. Temperature Dependent Quenching Rate Constants

Since heavy particle quenching affects the efficiency of these exciplex lasers, information on these rate constants is

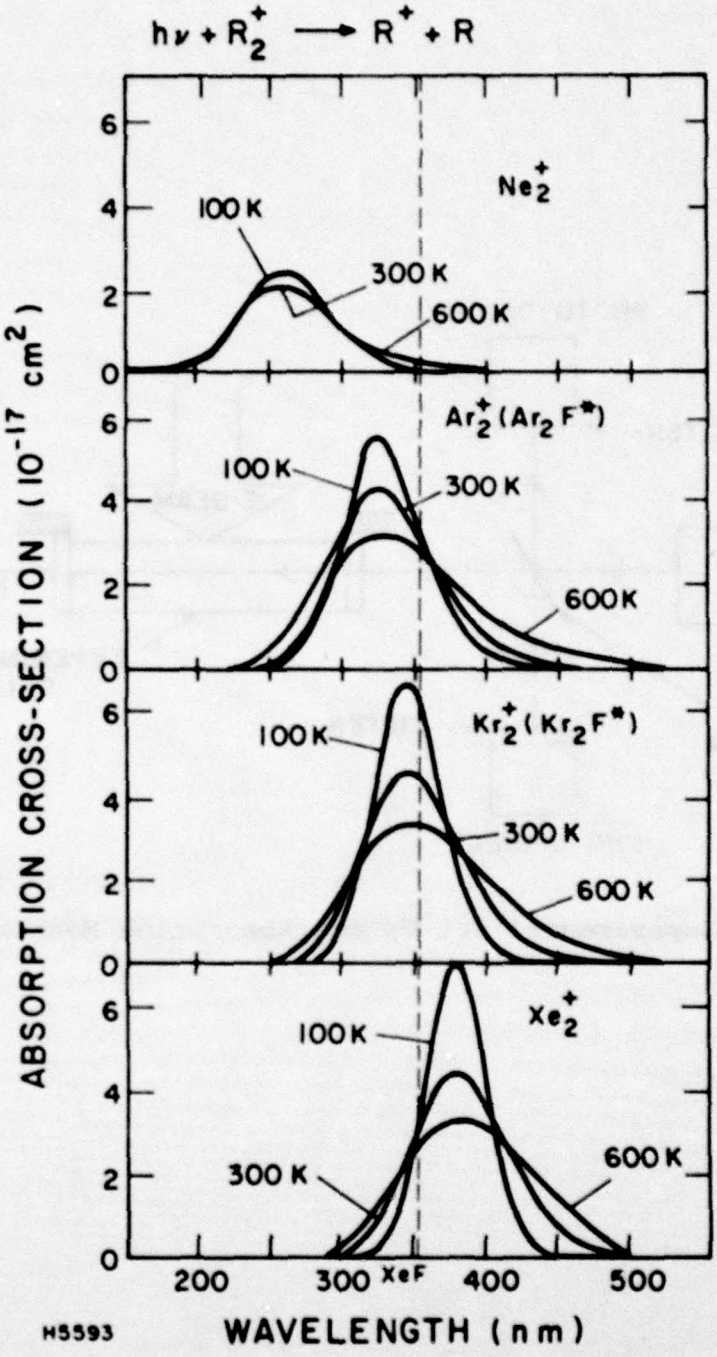

Figure 12 Photodissociation Cross Sections (Wadt, Cartwright and Cohen, App. Phys. Lett. 31, 672 (1977))

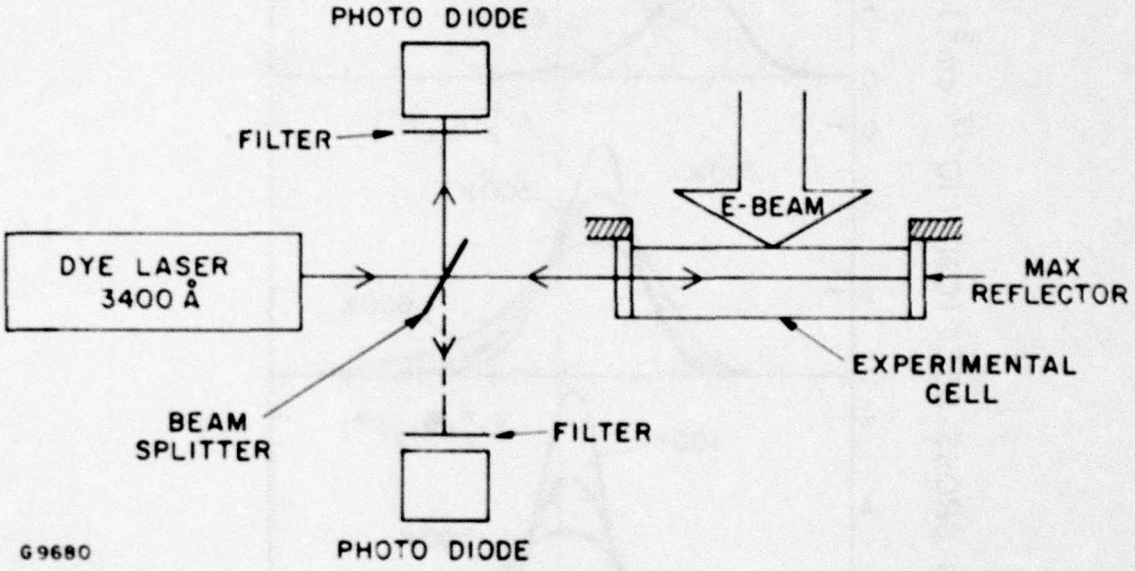

Figure 13 Experimental Set Up for Absorption Measurements

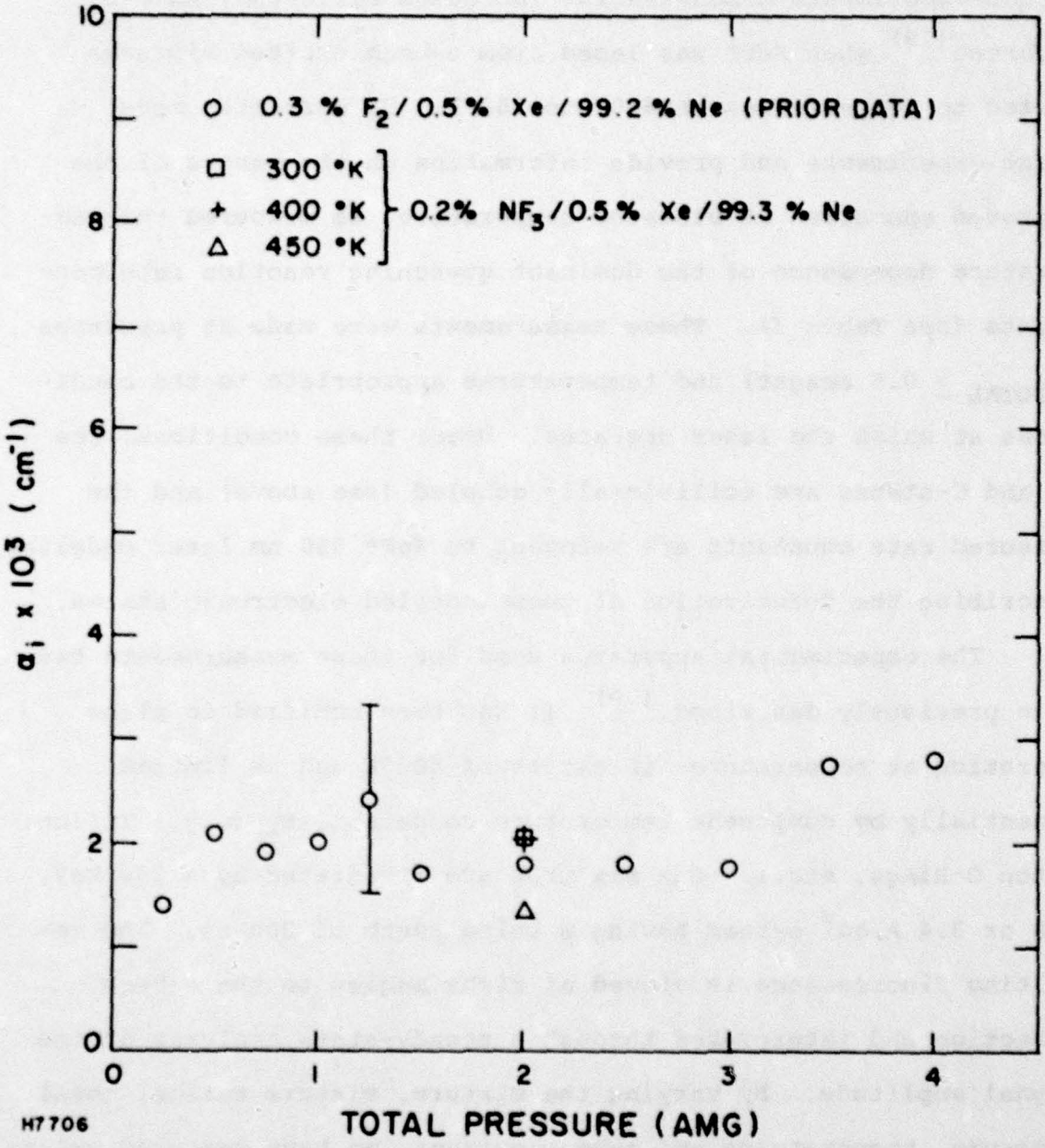

Figure 14 Excited State Absorption in Heated XeF* Laser Mixtures

necessary for predicting the laser's performance. In addition, recent experiments demonstrating increased efficiency have been reported[29] when XeF* was lased from e-beam excited mixtures heated to temperatures of 400° to 500°K. To correctly model these experiments and provide information on the causes of the improved operation at elevated temperature, we measured the temperature dependence of the dominant quenching reaction rate constants (see Table I). These measurements were made at pressures ($P_{TOTAL} \geq 0.5$ amagat) and temperatures appropriate to the conditions at which the laser operates. Under these conditions, the B- and C-states are collisionally coupled (see above) and the measured rate constants are relevant to XeF* 350 nm laser modeling describing the deactivation of these coupled electronic states.

The experimental apparatus used for these measurements has been previously described.[30] It has been modified to allow operation at temperatures in excess of 500°K and is limited essentially by component temperature compatibility (e.g., Teflon, Viton O-Rings, etc.). Gas mixtures are irradiated by a 150 keV, 0.8 or 3.4 A/cm^2 e-beam having a pulselength of 300 ns. The resulting fluorescence is viewed at right angles to the e-beam direction and interpreted through a steady-state analysis of the signal amplitude. By varying the mixture, mixture ratios, total pressure, temperatures and e-beam current, we have measured values for ($k\,\tau_{rad}$) for a variety of two- and three-body quenching processes, where k is the rate constant, and τ_{rad} is the spontaneous lifetime of XeF*. This product ($k\,\tau_{rad}$) is the relevant parameter

used for laser modeling. However, assuming a value of τ_{rad} of 16 ns, we have provided values for the two- and three-body quenching rate constants which are summarized in Table I at two different temperatures. These rate constants represent the first reported measurements of electron quenching of XeF* and the first temperature variation of these quenching processes.

a. Experimental

The apparatus is shown schematically in Figure 15. The spatially uniform high energy e-beam (from a broad area cold cathode consisting of a series of tantalum strips) impinges upon a thin (1 or 2 mil) Kapton foil. The reaction cell containing the reactant gas mixtures is constructed principally of stainless steel. The fluorescence is monitored at right angles to the e-beam direction by an optically filtered (see Figure 16), appropriately attenuated, photodiode (ITT F4502, S-4 response). The resutling signal is photographically recorded on an oscilloscope (Tektronix, 7844), see Figure 17. Viewing is restricted to a 1.5 mm slab immediately next to the foil. This insures that even at the highest pressures the gas mixture is a thin target and a one-dimensional treatment of the e-beam deposition is valid.

To obtain the quenching of XeF* by electrons, xenon and fluorine, the reactant gas consisted of binary mixtures of xenon and fluorine (0.2, 0.4, 0.6, 0.8 and 1% fluorine in 380, 570, 760, 1140 and 1570 torr of xenon). Once these rate constants were determined, ternary mixtures with varying amounts of neon were

TABLE I

SUMMARY OF QUENCHING RATE CONSTANTS

(τ = 16 ns)

	(T = 300°K)	(T = 500°K)
Two-Body Quenching (cm^3/s)		
$XeF^* + e$	$4.0 \times 10^{-7\dagger}$	$8.3 \times 10^{-7\dagger}$
$+ F_2$	1.5×10^{-10}	1.7×10^{-10}
+ Xe	1.8×10^{-11}	0.62×10^{-11}
+ Ne	Negligible	Negligible
Three-Body Quenching (cm^6/s)		
$XeF^* + Xe + Xe$	2.6×10^{-31}	2.2×10^{-31}
+ Ne	7.9×10^{-31}	11×10^{-31}
$+ F_2$	1.5×10^{-29}	0.79×10^{-29}
+ Ne + Ne	4.5×10^{-33}	5.8×10^{-33}

† Reduction of Data Assumes Dissociative Attachment Rate Constant of $k = 4.5 \times 10^{-9}$ cm^3/s at 300°K and 5.7×10^{-9} cm^3/s at 500°K for $e + F_2$

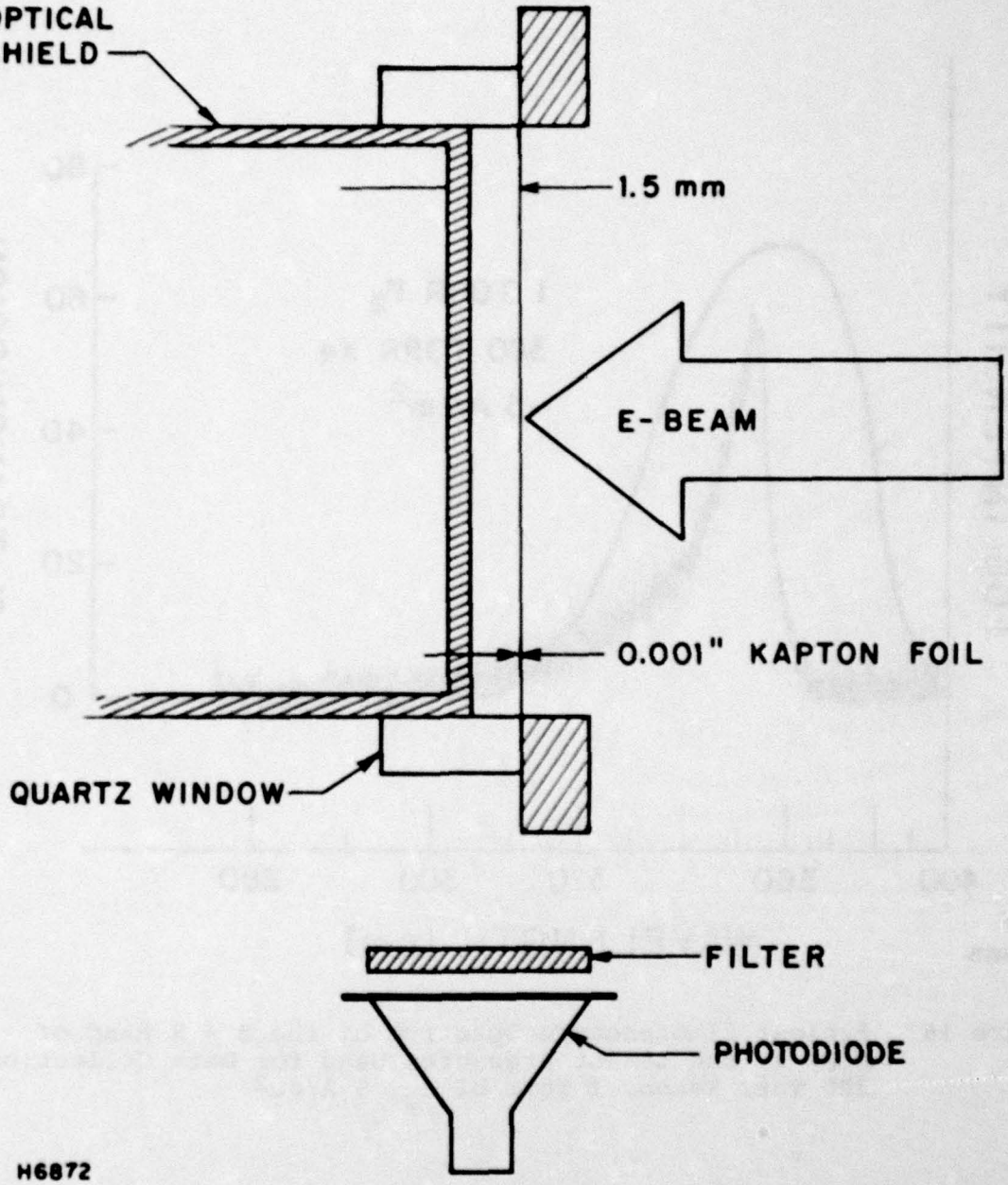

Figure 15 Schematic of Experimental Setup

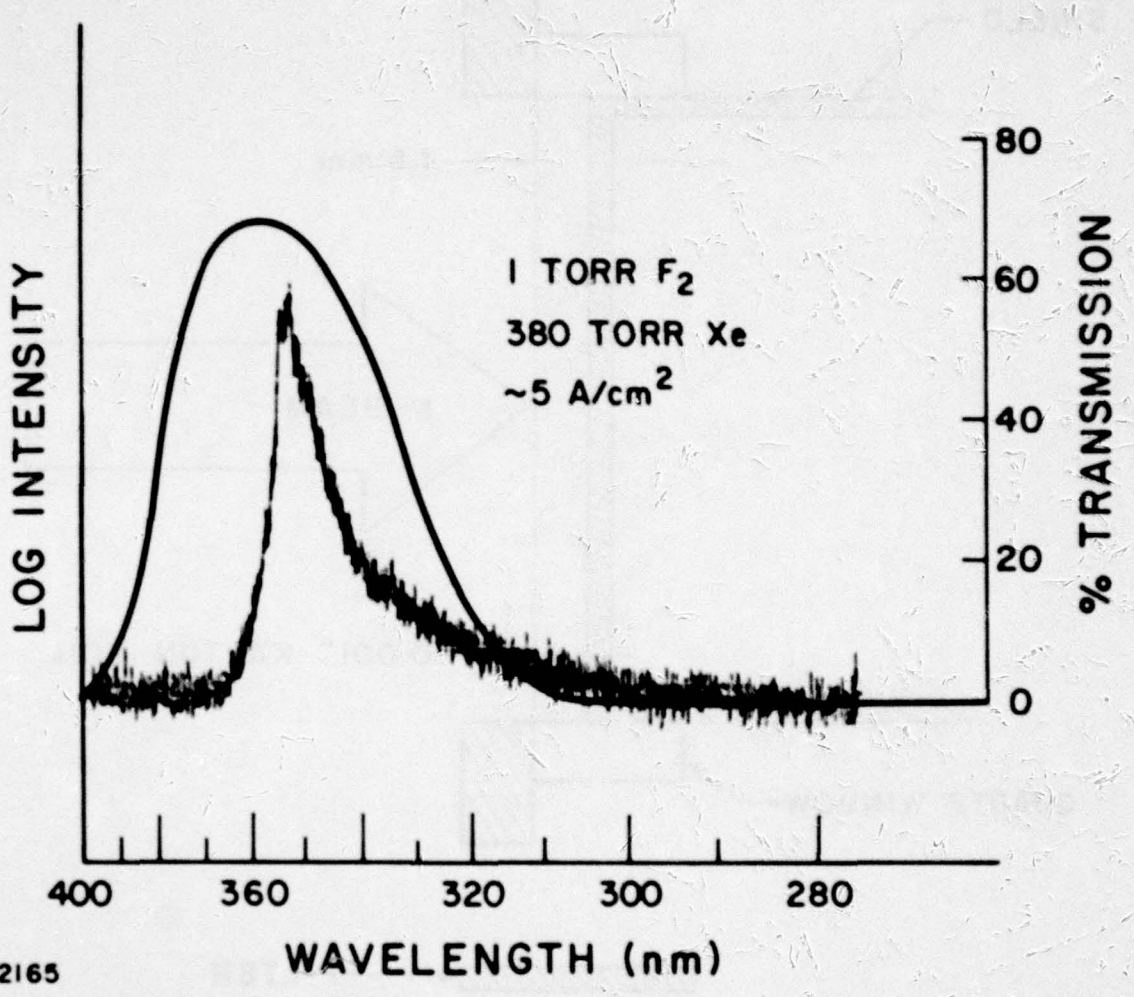

Figure 16 Typical Fluorescence Spectrum of the B → X Band of XeF* at the Lowest Pressures Used for Data Collections: 380 Torr Xenon, 1 Torr of F_2, 5 A/cm^2

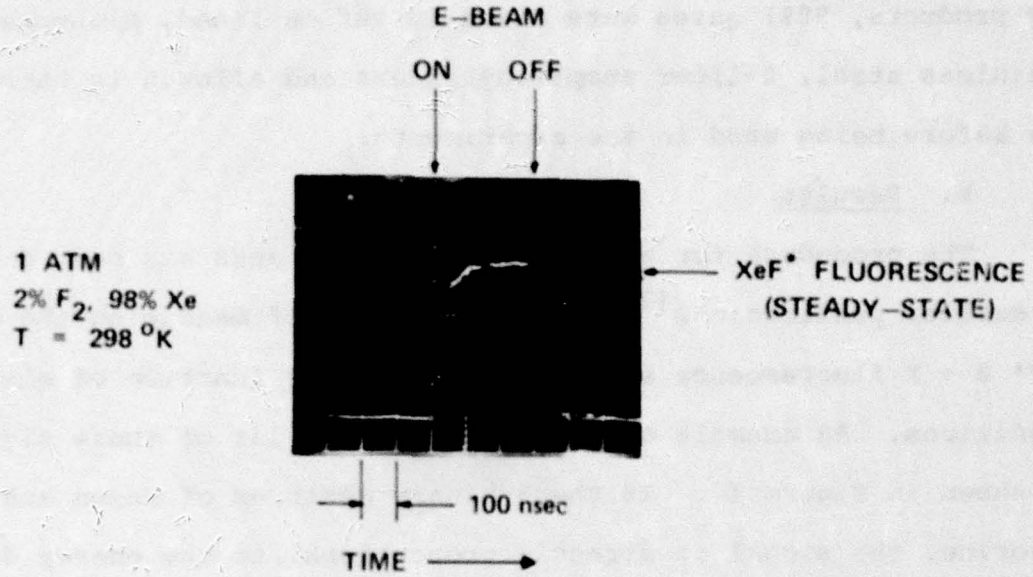

H6876

Figure 17 XeF*(B → X) Fluorescence Signal as f (time)

investigated to obtain two- and three-body quenching rate constants of XeF* involving neon (F_2 fixed at 0.3%, Xe fixed at 2 or 5% with the balance of neon to total densities of 3040 torr). The neon (Cryogenic, 99.999%) xenon (Cryogenic, 99.9995%) and fluorine (AR products, 98%) gases were mixed in Teflon-lined, high-pressure, stainless steel, 5-liter sample cylinders and allowed to thoroughly mix before being used in the experiments.

b. Results

The procedure for extracting rate constants has been described in earlier publications[30,31] and consists of measuring the observed XeF* B → X fluorescence signal amplitude as a function of mixture conditions. An example of the temporal behavior of these signals is shown in Figure 17. In these binary mixtures of xenon and fluorine, the signal is directly proportional to the energy deposition (i.e., the xenon density) and inversely proportional to the various quenching processes as follows:

$$\text{signal} = \frac{\alpha N_{Xe}}{1 + \tau_{rad}\left(k_{F_2} N_{F_2} + k_{Xe} N_{Xe} + k_{el} N_{el} + k_{2Xe} N_{Xe}^2 + k_{Xe,F_2} N_{Xe} N_{F_2}\right)}$$

where τ_{rad} is the XeF* spontaneous liftime, k_{F_2}, k_{Xe}, k_{el}, etc., are the rate constants describing the various processes and the N's are the densities of the various components. By operating at fixed xenon density (200 torr) and varying the amount of fluorine for a given e-beam current (see Figure 18), we obtained information about the two- and three-body quenching involving F_2, i.e.,

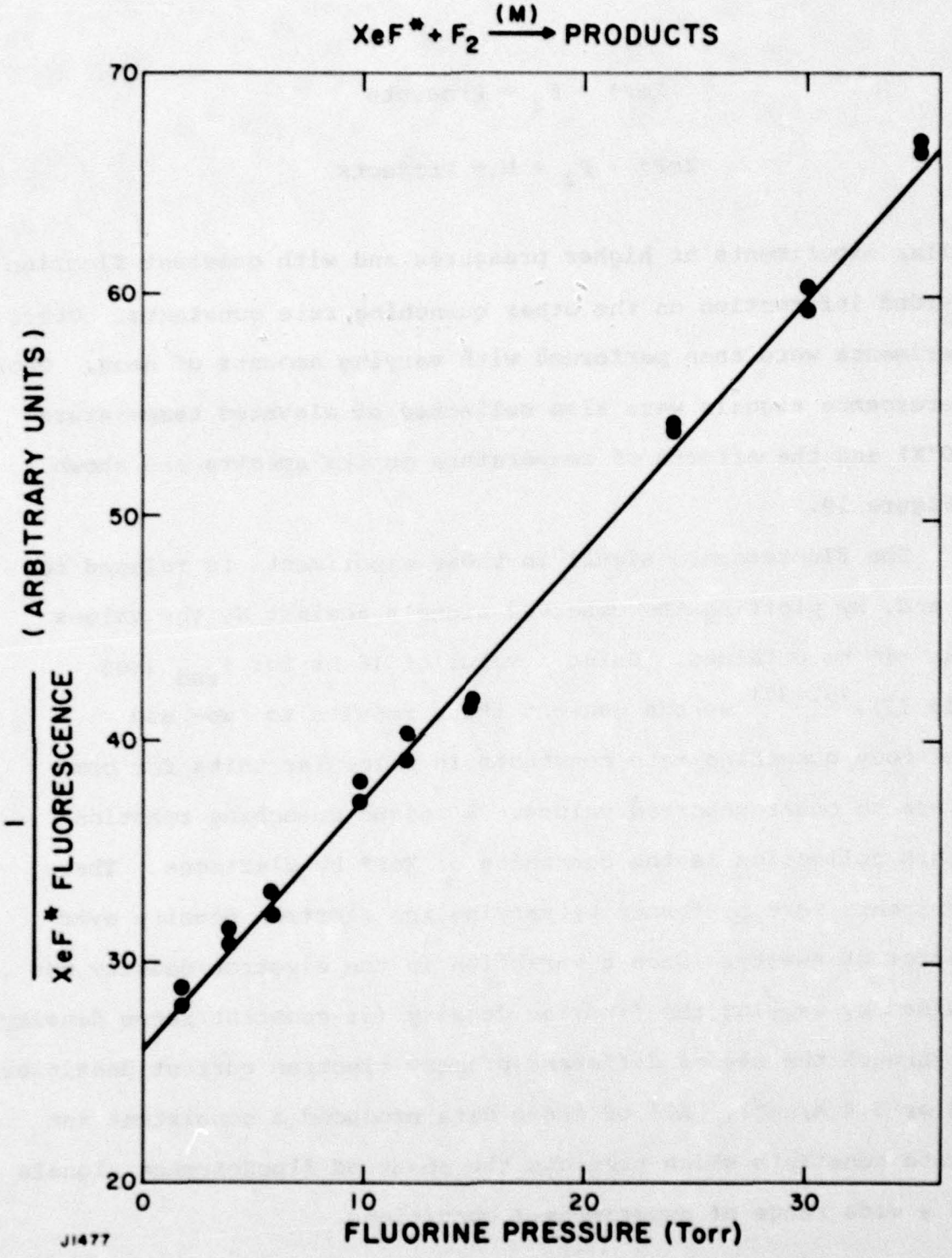

Figure 18 (XeF* Fluorescence)$^{-1}$ vs F_2 Density

$$XeF^* + F_2 \rightarrow \text{Products}$$

$$XeF^* + F_2 + M \rightarrow \text{Products}$$

Similar experiments at higher pressures and with constant fluorine provided information on the other quenching rate constants. Other experiments were then performed with varying amounts of neon. These fluorescence signals were also collected at elevated temperature (500°K) and the effects of temperature on the spectra are shown in Figure 19.

The fluorescence signal in these experiments is related to $k_\tau N$ and, by plotting the observed signals against N, the values of k_τ can be obtained. Using a value of 16 ns for τ_{rad} (see Table II),[32-37] we can convert these results to two- and three-body quenching rate constants in molecular units for comparison to other reported values. A unique quenching reaction in this collection is the quenching of XeF* by electrons. These experiments were performed by varying the electron density over a factor of twenty. Such a variation in the electron density was obtained by varying the fluorine density (at constant xenon density) and through the use of different primary electron current densities (0.8 or 3.4 A/cm^2). All of these data produced a consistent set of rate constants which predicts the observed fluorescence signals over a wide range of experimental conditions.

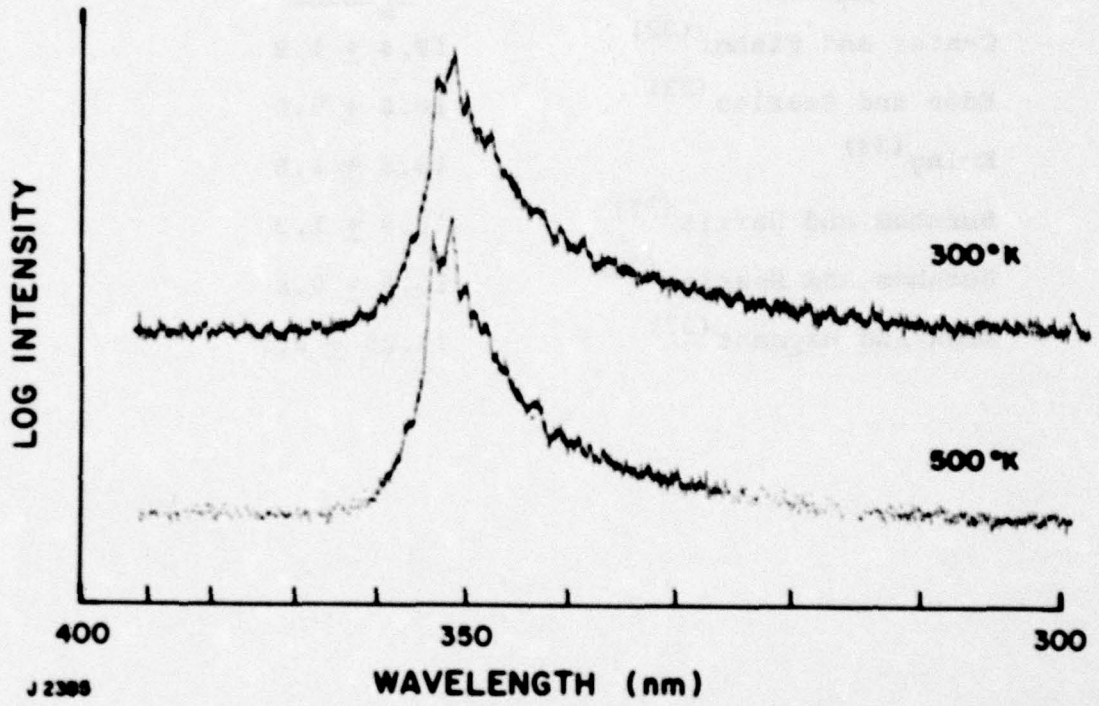

Figure 19 Fluorescence Spectra of the B → X Band of XeF* at Two Gas Temperatures: 300 and 500°K. Experimental conditions were 0.5% F_2, balance xenon at total pressures of 0.5 Amg.

TABLE II

SUMMARY OF EXPERIMENTAL VALUES OF
XeF (B) RADIATIVE LIFETIME

Author	τ_B (ns)
Center and Fisher[32]	19.4 ± 1.0
Eden and Searles[33]	16.0 ± 5.0
Ewing[34]	13.5 ± 1.0
Burnham and Harris[35]	18.8 ± 1.3
Burnham and Searles[36]	15.0 ± 0.8
Eden and Waynant[37]	14.25 ± 0.2

c. Discussion

For comparison, we show in Table III our present measurements for the quenching processes

$$XeF^* + Xe \rightarrow \text{Products}$$

$$+ F_2 \rightarrow \text{Products}$$

with those of others.[32,37,38] Also, we can compare the values for the three-body quenching rate constants reported earlier[30] to those obtained here for the reactions.

$$XeF^* + Xe + Ne \rightarrow$$

$$+ Ne + Ne \rightarrow$$

$$+ Xe + Xe \rightarrow$$

These are summarized in Table IV. With the exception of the three-body rate constants for quenching of XeF* by xenon with xenon as the third-body reported by Eden and Waynant,[37] the agreement among these reported rate constants is within a factor of two. The exceptionally high value reported by these workers[37] is in disagreement with our results and recent theoretical predictions.[39] However, it has also been reported[38] that under different experimental conditions no evidence of three-body quenching was observed to pressures near 700 torr.

With regard to theoretical expectations concerning the temperature effect on these rate processes, a simple model would anticipate the two-body heavy particle quenching to increase with a $T^{1/2}$ dependence, if the relaxation processes involve impulsive collisions and no complex formation. On the other hand, all

TABLE III

QUENCHING RATE CONSTANTS XeF*
(cm^3/s)

Quencher	Present Work	Center & Fisher[32]	Brashears & Setser[43]	Eden & Waynant[37]
Xe	1.8×10^{-11}	6.0×10^{-11}	6.0×10^{-11}	3.3×10^{-11}
F_2	1.5×10^{-10}	1.2×10^{-10}	2.0×10^{-10}	3.8×10^{-10}
Ne	Negligible	$< 3 \times 10^{-13}$		7.7×10^{-13}

TABLE IV

QUENCHING RATE CONSTANTS, XeF*
(cm^6/s)

Quenching Reaction	This Work	Rokni et al.[30]	Eden/Waynant[37]
XeF* + Xe + Ne	7.9×10^{-31}	7.8×10^{-31}	
+ Ne + Ne	4.5×10^{-33}	2.5×10^{-33}	
+ Xe + Xe	2.6×10^{-31}		2.4×10^{-29}

three-body reactions are believed to proceed via complex formation and one would expect these rate constants to exhibit a "negative temperature dependence," perhaps $T^{-1/2}$. Clearly, the data show some exceptions to these anticipated trends.

There are no comparable results for electron quenching of XeF* with which to compare. Results reported on modeling of discharge excited KrF* lasers suggest, for model agreement with observed laser performance, a value of 6×10^{-7} cm^3/s was required.[40] Clearly, a rate constant of this magntiude implies electrons may be a significant source of quenching under conditions where the electron density is relatively high. The sensitivity of our data to electron quenching can be seen by comparing fluorescence signals to model predictions using the rate constants summarized in Table I including and excluding electron quenching of XeF* (see Figure 20). These data also clearly show the effect at high pressure of three-body quenching. The rate constants for electron quenching were deduced in the same way as the neutral particle quenching, but the correlation between the observed signal and the rate constant is more circuitious. In Figure 21 is a plot of 1/signal (corrected for quenching involving fluorine) vs secondary electron density, n_e. n_e for attachment dominated conditions is proportional to the production of electrons by fast electrons interacting with the xenon buffer gas, S_{eb}, and the rate of removal of these secondary electrons by dissociative attachment with the fluorine molecules present, viz,

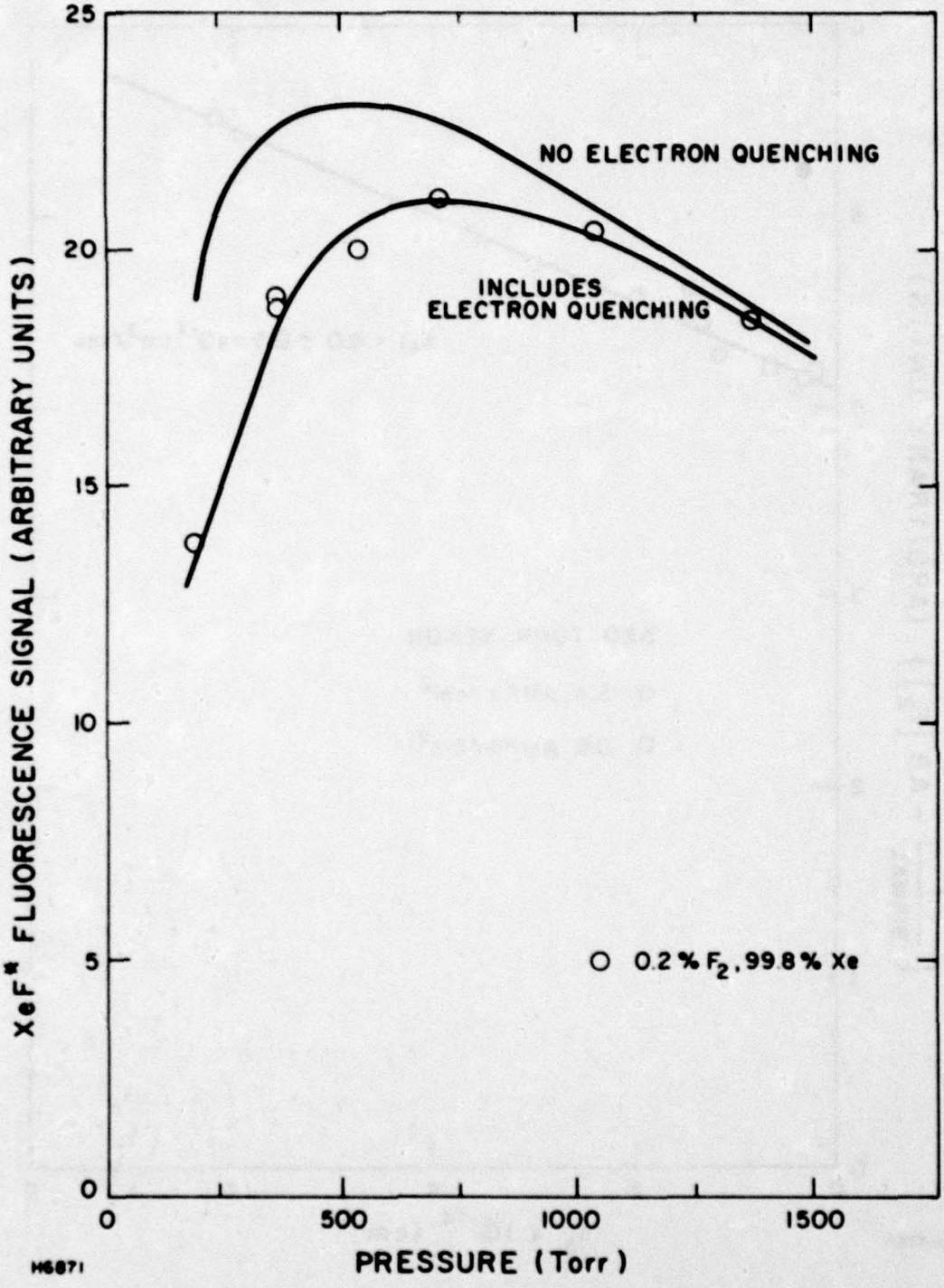

Figure 20 Rate Constant Model Calculation Fit to the Data

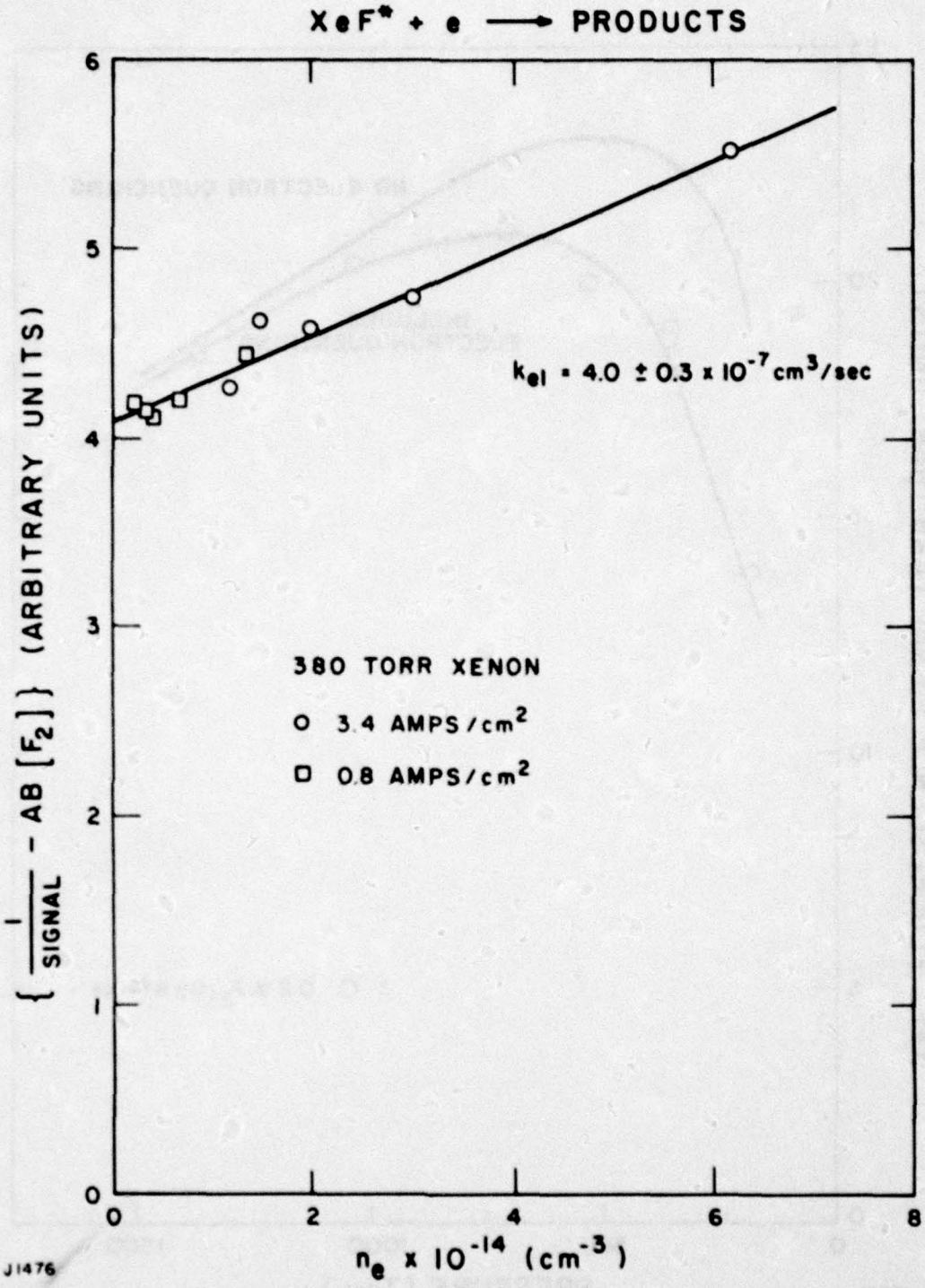

Figure 21 (XeF* Fluorescence Corrected for F_2 Quenching)$^{-1}$ vs Electron Density Where A is a Calibration Factor Containing the Source Term and Geometry Considerations and B = $k_{F_2} \tau_{rad}$

$$\frac{d[n_e]}{dt} = S_{eb} - k_a\ [n_e]\ [F_2]$$

Under steady-state conditions (see Figure 17),

$$n_e = S_{eb}/k_a\ [F_2]$$

The dissociative attachment rate constant, k_2, is a function of both the electron and fluorine energies. We have used a value of 4.5×10^{-9} cm^3/s for this rate constant at 300°K and 5.7×10^{-9} cm^3/s at 500°K for our experimental conditions (~ 1 eV mean electron energy) based on recent experimental data on electron attachment.[41] Due to the relationship between n_e and this attachment rate constant, the value for the electron quenching reported here will be proportional to k_a. For example, revision of these rate constant values assumed for $e + F_2$ upward will cause the rate constants for $e + XeF^*$ to scale in the same manner.

The likely physical processes represented by electron quenching under our experimental conditions may involve any or all of the following product channels:

a) Electron dissociative attachment

$$XeF^* + e \rightarrow Xe^* + F^-$$
$$\rightarrow Xe + F^-$$

b) Superelastic collisions

$$XeF^* + e \rightarrow XeF\ (X) + e'$$
$$\rightarrow Xe + F + e'$$

Experiments on the temperature effect on various dissociative attachment processes have shown increased rate constant values as higher vibrational states are assessed and, therefore, electron attachment could provide a mechanism whereby a thermal temperature effect could be anticipated,[41,42] but the magnitude of the observed rate constant appears quite large for an attachment mechanism (for average electron energies near 1 eV) and, therefore, not likely to be the dominant processes. No strong temperature effect on the rate constant would be anticipated via the superelastic channel, yet this channel, depending on the products, would have the most significant impact on XeF* laser operation (see below) due to the decrease in the inversion density as a result of increasing the lower laser level population. However, one mechanism that can qualitatively explain this apparent temperature effect would be if the higher lying electronic state (e.g., the XeF B-state) has a significantly larger electron quenching rate constant than the lower lying state. The observed increase in the rate constant from 4.0×10^{-7} cm^3/s at 300°K to 8.3×10^{-7} cm^3/s at 500°K would then be a reflection of thermal population shifts between the collisionally coupled electronic states and their respective rotational/vibrational mainifolds.

In general, these data show that for typical laser mixtures electron quenching is a dominant loss process (see Figures 22 and 23) accounting for more than 40% of the quenching losses at optimum temperature.

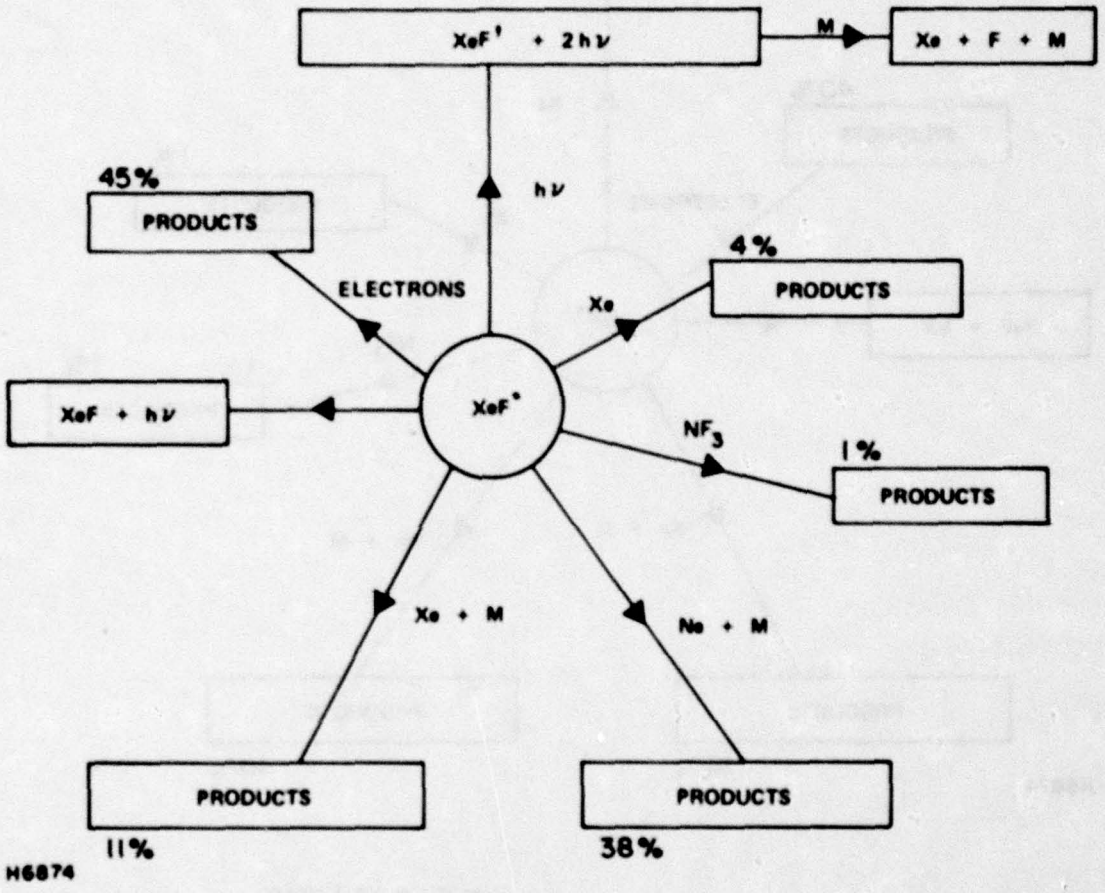

• τ_q = 16.0 nsec

Figure 22 Dominant Quenching Kinetics T = 298°K

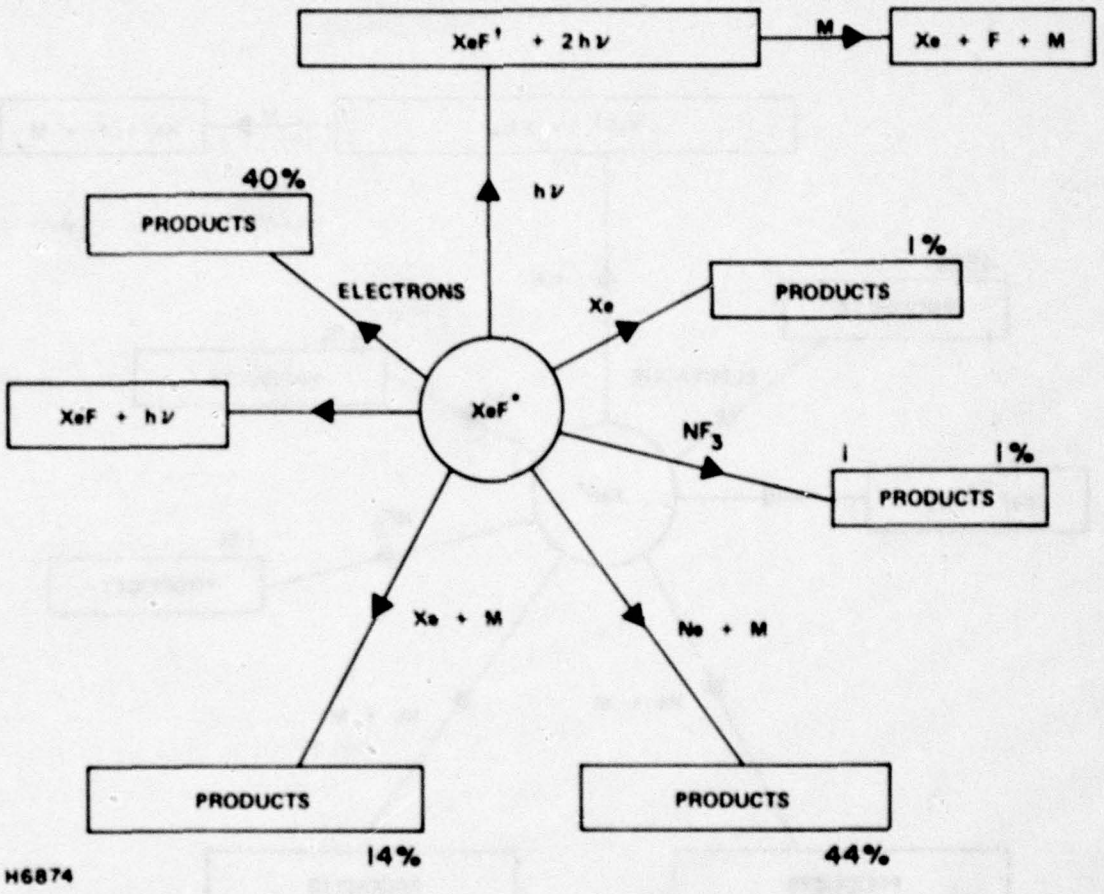

• τ_q = 14.1 nsec

Figure 23 Dominant Quenching Kinetics T = 500°K

4. The Effect of Ground State Population on the XeF Laser Performance

One of the reasons that exciplex lasers have demonstrated exceptional performance is that the lower level is repulsive and hence an inversion will automatically exist provided the upper level can be populated. Unfortunately XeF is an exception to this rule. The lower level of XeF(X) is bound by about 0.15 eV.[44] At room temperature and under equilibrium conditions most XeF molecules would be dissociated to atomic Xe and F.[45] To predict the laser output flux it is necessary to determine the rate of dissociation of XeF(X). Clearly, the more rapid the dissociation the more efficient the XeF laser. Recently Fulghum et al.[46] reported measurments of the XeF ground state dissociation rate with He as a buffer gas. In this work, we investigate the bottlenecking effect due to the finite ground state lifetime of XeF for typical laser mixtures at room temperature and at 500°K.

At room temperature the dominant laser transition is XeF (B,v' = 0) → XeF(X,v" = 3). Figure 24 shows the potential curves of the upper and lower laser levels and the dominant transitions. Experimentally, the effect of the finite lower level lifetime on the laser performance can be investigated by observing the sidelight fluorescence under lasing and non-lasing conditions. The fluorescence will, of course, be proprotional to the upper level density. By considering the rate equations of the upper and lower levels one can show that

$$\frac{N^*}{N_o^*} = \left(1 + \frac{1}{\beta}\frac{\phi}{\phi_s}\right)\left(1 + \frac{\phi}{\phi_s}\right)^{-1} \qquad (2)$$

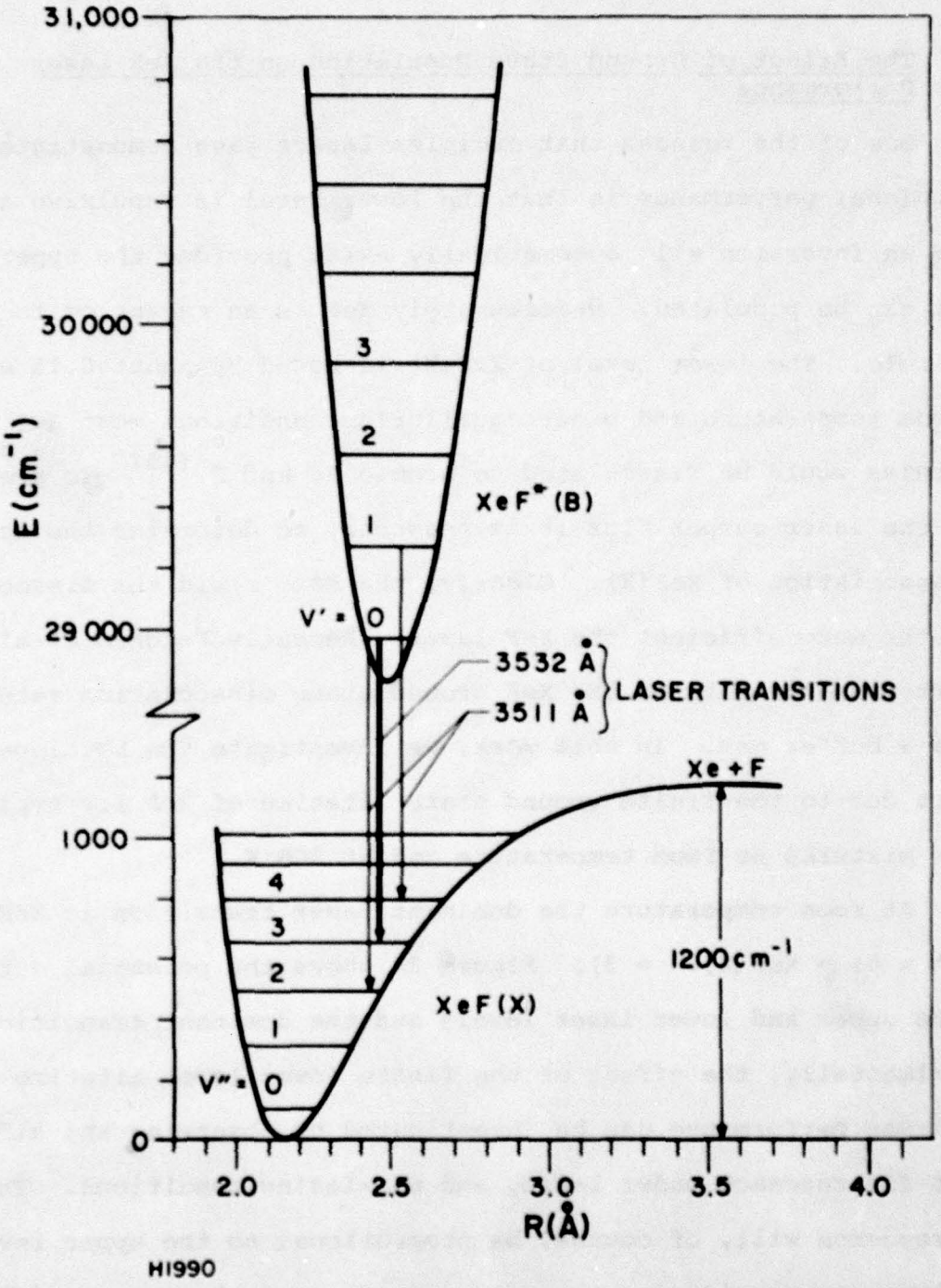

Figure 24 Potential Energy Diagram for XeF Indicating the Laser Transitions

where N^* is the population of the zeroth vibrational level of the B-state. N_o^* is the population when the cavity flux ϕ is zero. ϕ_s is the saturation flux which is defined as the flux at which the gain is decreased by a factor of two. β is a function of the upper and lower level lifetimes, the vibrational relaxation times of the upper level and lower level manifolds and the distribution functions of these levels. As the lower level lifetime approaches zero β approaches infinity. Once β is determined the extraction efficiency of the XeF* laser can be accurately calculated.[6] Equation (2) is derived without assuming vibrational equilibrium of the electronic states, but we have assumed that the rotational relaxation is extremely rapid compared to the upper level lifetime and the dissociative lifetime of the lower level.[47]

For conditions where the upper and lower level manifold are each in vibrational equilibrium, β is given by

$$\beta \approx 1 + \tau_u \left(\frac{\theta_{uv}}{\theta_{\ell 3} \tau_\ell} - \frac{1}{\tau_{u\ell}} \right) \tag{3}$$

where τ_u and τ_ℓ are the lifetimes of the upper and lower levels, respectively, $1/\tau_{u\ell}$ is the rate of transitions from upper level mainifold to the lower level manifold, θ_{uo} (= 0.77) is the fraction of the upper level population that is in the v' = 0 level and $\theta_{\ell 3}$ (= 0.026) is the fraction of the lower level population that is the v" = 3 level of 300°K.

A schematic of the experimental setup is shown in Figure 25. The laser mixture contained 0.2% NF_3, 0.5% Xe and 99.3% Ne at a total pressure of 3 atm and was excited by a 150 keV beam of electrons. The details of the e-beam and gas cell have been described previously.[1] To obtain a large ratio of ϕ/ϕ_s, the e-beam current density was maintained at 41 A/cm^2. The laser cavity was formed by a maximum reflector and a 95% output coupler. The maximum reflector had a radius of curvature of 4 m, while the output coupler was flat. The cavity flux was altered by introducing varying amounts of chlorine into an absorption cell which was placed in the optical cavity. The cavity flux near the output coupler was determined by measuring the transmitted flux through the 95% mirror using a calibrated photodiode. The sidelight was monitored at the active region nearest the output coupler as shown in Figure 25. The intracavity flux at the viewing port was varied from 0 to 6 MW/cm^2. Since there are two laser emissions lines, a filter, having a bandpass of 10 Å, centered at 353 nm (which corresponds to the 0-3 transition), was placed in front of the photodiode. The cross section of the active medium was 1 cm^2 and the mode volume was ~ 60 cm^3.

The experimental results are plotted in Figure 26 which shows the variation of N_o^*/N^* as a function of the measured cavity flux. This ratio saturated verifying that XeF(X) has a finite lifetime. The curve in that figure is a best fit of the data to Eq. (3). From Figure 26 we obtain a value of $\beta \approx 1.6$. One can also estimate the saturation flux from the data shown in Figure 16 to be

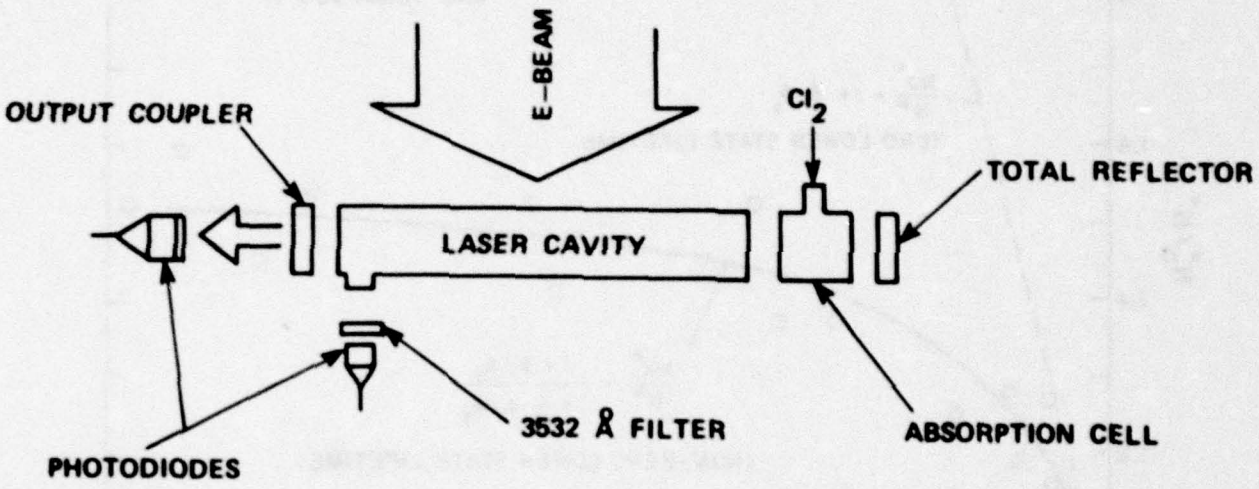

Figure 25 Schematic of the Experimental Setup

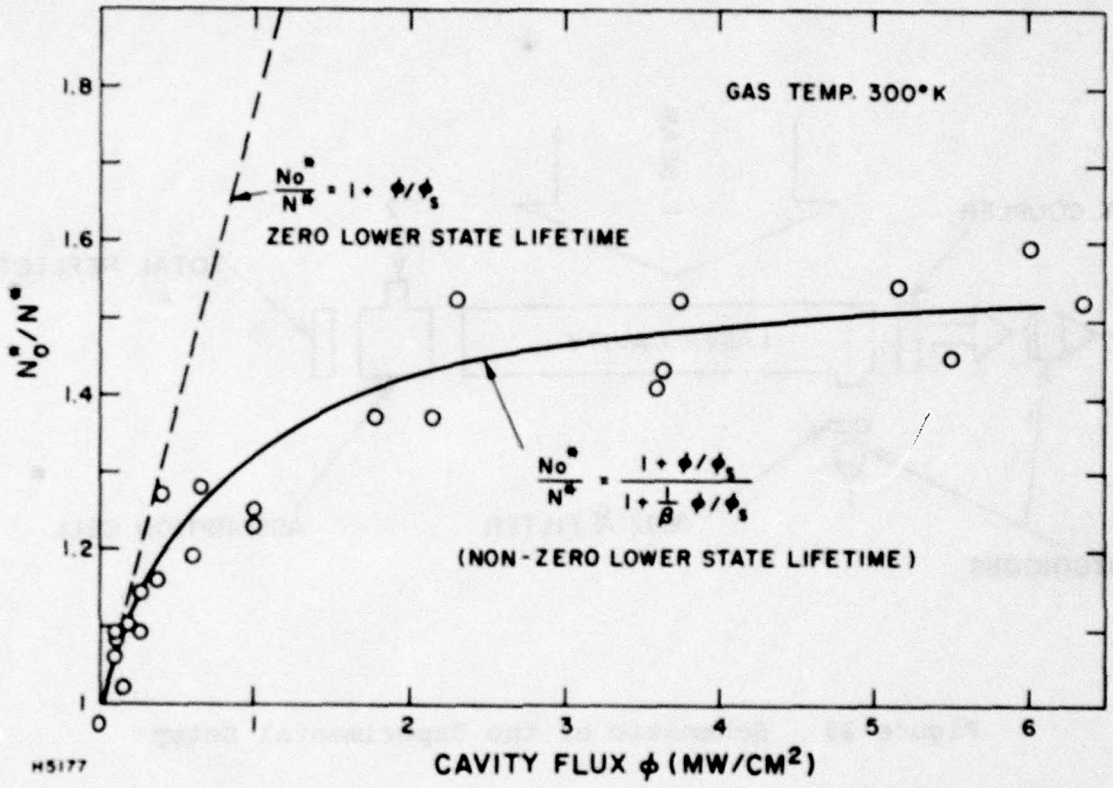

Figure 26 The Ratio of N_o^*/N^* as a Function of Cavity Flux. The solid line is the best fit of the data to Eq. (2).

0.6 MW/cm^2. The saturation flux assuming complete vibrational realxation is given by:

$$\phi_s \approx \frac{h\nu}{\sigma\tau_u}\left[\theta_{uo} + \theta_{\ell 3}\left(\frac{\tau_\ell}{\tau_u} - \frac{\tau_\ell}{\tau_{u\ell}}\right)\right]^{-1} \qquad (4)$$

Using the measured quenching rates (see above), we can calculate for our experimental conditions τ_u = 3.8 ns, where the dominant quenching is due to electrons. If we assume that all of the electron quenching results in the following process

$$e + XeF(B) \rightarrow e + XeF(X)$$

then $\tau_{u\ell}$ = 4.4 ns.

Using these values of τ_u and $\tau_{u\ell}$ we can estimate, from Eq. (3) τ_ℓ to be 77 ns. Taking ϕ_s = 0.6 MW/cm^2, we can then compute the stimulated gain cross section from Eq. (4) to be about 2.9 x 10^{-16} cm^2.[47-49] At the other extreme, the electron quenching process could result in atomic Xe and F. For this case $\tau_{u\ell}$ is just radiative lifetime of 16 ns. Then, from Eq. (3), we obtain τ_ℓ to be 135 ns. For this case σ is found to be 1.7 x 10^{-16} cm^2. The reason that quasi-steady-state lasing is possible even though the lower level lifetime is so much greater than the upper level lifetime is that the laser transition terminates on the third vibrational level and the lifetime of this level is shorter than the upper level lifetime. In computing the lower level lifetime, we have assumed that the upper and lower levels are in vibrational equilibrium with the

gas. From previous data we know that this is not the case.[6] So these evaluations are probably upper bound estimates. It is interesting to note that Fulghum et al.[46] would predict a τ_ℓ of 44 ns if the buffer gas was He at 3 atm and not Ne.

If the temperature of the mixture is raised, one would expect τ_ℓ to decrease. Figure 27 shows the effect of increased temperature on the lower state lifetime. Results at 300° and 500°K are presented. These experiments were performed for the same mixture and density as those presented in Figure 26. The e-beam current density for this set of experiments was 25 A/cm^2. The asymptote for the room temperature data in Figure 27 is higher than that in Figure 26. This is due to the decrease in the electron quenching corresponding to the lower e-beam current used in this set of experiments.

For a given cavity flux, N_o^*/N^* is larger for the higher temperature data. From the data presented in Figure 27, it is obvious that β will be considerably larger for the 500°K case. Since the electron quenching is dominant, the increase in the value of β is mainly due to the increased dissociation rate of the ground state. This is in agreement with the theoretical expectations of Shui and Duzy.[50]

Detailed analysis shows[6] that due to the ground state bottlenecking, the extraction efficiency of the XeF laser is decreased by the factor $(1 - \frac{1}{\beta})$. From Figure 27, one can estimate for β a value of ~ 1.8 at 300°K and ~ 3.5 at 500°K. Thus,

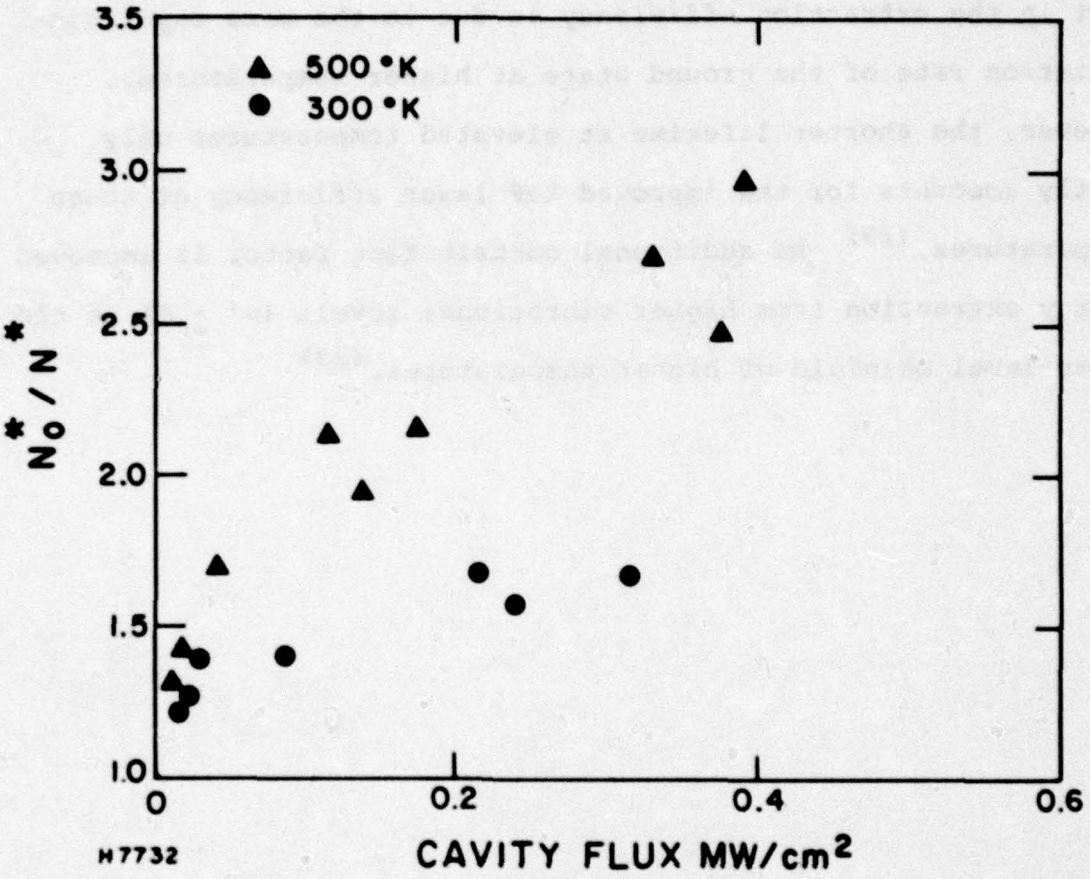

Figure 27 The Ratio of N_o^*/N^* as a Function of Cavity Flux for Gas Temperatures of 300°K and 500°K. The e-beam current density was 25 A/cm². The solid curves are the best fit to the data of Eq. (2).

for the experimental conditions of Figure 27, an increase by a factor of 1.5 in the extraction efficiency is expected, when the gas temperature is raised from 300° to 500°K. This improvement in the extraction efficiency is due to the more rapid dissociation rate of the ground state at higher temperatures. However, the shorter lifetime at elevated temperatures only partly accounts for the improved XeF laser efficiency at these temperatures.[29] An additional contributing factor is improved energy extraction from higher vibrational levels ($v' \geq 1$) in the upper level mainfold of higher temperatures.[29]

C. PULSE SHAPE AND LASER ENERGY EXTRACTION FROM E-BEAM PUMPED KrF*

The physical processes which determine the performance of KrF* lasers have been intensively researched during the last two years. As a result of this research, for e-beam excitation intensities in the 1-5 x 10^5 W/cm^3 regime, the dominant formation and quenching kinetics are well understood,[51,52] the stimulated cross section has been measured, and the dominant absorbers in the active medium has been identified.[27] The above information allows one to construct a comprehensive model which can be used to predict laser performance over a wide range of laser operating conditions. Experimental verification of the predictive capability of such a model then provides an independent check on the various kinetics leading to medium gain and absorption, as well as a check on the validity of power extraction model.

In this section, a description of such a code is presented. The predictions of the code are compared with experimental results obtained with a 1-m e-beam excited KrF* laser device. The comparison includes the temporal shape of the KrF* laser output and sidelight pulses, the output pulse energy, and intrinsic laser efficiency. Also included is a detailed description of the 1-m laser device. The model predicts the laser energy and power extracted and efficiencies to within 10% of the experimental values. A detailed comparison of the predicted and measured sidelight emission, however, show evidence of processes not previously addressed. These include (a) the effect of finite vibrational relaxation and (b) electron quenching of KrF*. Although for the

experimental conditions discussed in this section the effect of these processes on the overall laser performance is about 10%. They may become important at pump powers > 5 x 10^5 W/cm^3.

In the following discussion we summarize the formation and quenching kinetics. Then we discuss how the kinetics are coupled to power extraction by the laser cavity flux and the experimental apparatus and a detailed comparison between the results and model are presented. Finally, a discussion of the processes not previously investigated will be addressed and a scaling map for the KrF* laser is presented.

1. KrF* Laser Kinetics

Figure 28 shows a block diagram which summarizes the important processes included in the computer code. The e-beam energy results in the formation of electron and rare gas ion pairs. The secondary electrons are rapidly lost via dissociative attachment with the halogen donor to form F^-. These ionic states eventually result in the formation of KrF*.[51] The dominant formation kinetics and corresponding rates are listed in Table V (Refs. 53-56). Once the KrF* is formed, it can radiatively decay, be quenched by the rare gases or halogen donor or be stimulated by the cavity flux. The rate constants for the dominant formation and quenching processes have been measured and checked by comparing the measured KrF* fluorescence efficiency calculated using these rates for various Ar/Kr/F_2 mixtures. The dominant quenching reactions and rate constants used in the code are given in Table VI (Refs. 51 and 57). Inclusion of these processes also enables the code to

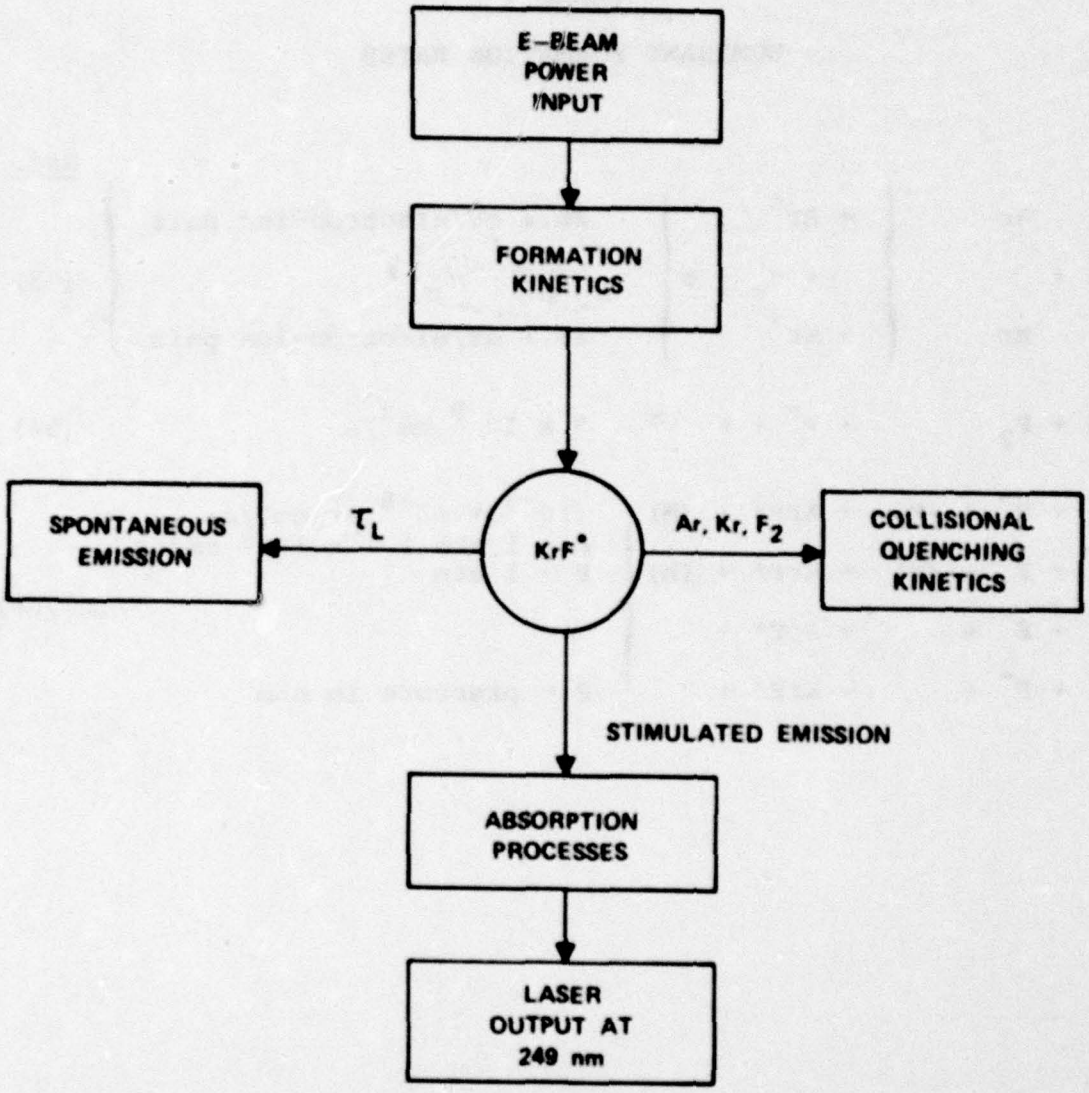

Figure 28 A Block Diagram of the KrF* Laser Code

TABLE V

DOMINANT FORMATION RATES

		Ref.
$\vec{e}$ + Ar → Ar^+ + e_s + e	26.4 eV/electron-ion pair	(53)
$\vec{e}$ + Kr → Kr^+ + e_s + e	24.1 eV/electron-ion pair	(53)
$e + F_2 \rightarrow F^- + F$	$\approx 3 \times 10^{-9}$ cm^3/s	(54)
$Ar^+ + F^- + (M) \rightarrow ArF^* + (M)$	$(10^{-7} + 10^{-6}\ P)$ cm^3/s; $P \leq 1$ atm 1.1×10^{-6} cm^3/s $P > 1$ atm	(55,56)
$Kr^+ + F^- + (M) \rightarrow KrF^* + (M)$		(55,56)
$Ar_2^+ + F^- \rightarrow ArF^* +$		(55,56)
$Kr_2^+ + F^- \rightarrow KrF^* +$	P = pressure in atm	(55,56)

TABLE VI

DOMINANT QUENCHING RATES

			Ref.
$KrF^* + F_2$	→ Products	7.8×10^{-10} cm^3/s^{-1}	(57)
$KrF^* + 2Kr$	→ $Kr_2F^* + Kr$	6.7×10^{-31} cm^6/s^{-1}	
$KrF^* + Kr + Ar$	→ $Kr_2F^* + Ar$	6.5×10^{-31} cm^6/s^{-1}	
$KrF^* + 2Ar$	→ Products	7×10^{-32} cm^6/s^{-1}	

predict the number densities of species which absorb at the laser wavelength. The calculated medium absorption has been compared with measured values for various mixtures and e-beam excitation levels.[27] The three important absorbing species are F_2, F^- and Kr_2F^*. The absorption cross sections of these species[27,58,59] are listed in Table VII. The molecular ions Ar_2^+ and Kr_2^+ also absorb[60] KrF* photon; however, their absorption is small compared to F_2, F^- and Kr_2F^*. What remains to be verified is the ability of the code to predict power extraction in the presence of intrinsic medium absorption and overall laser performance for various levels of e-beam excitation and laser gas mixtures. In the following section this ability is checked by comparing the predictions with experimental results. This comparison provides a verification of the validity of the power extraction model as well as an independent check of the various kinetics leading to laser medium gain and absorption.

2. Power Extraction

The rate of change of the cavity flux is given by

$$\frac{\partial \phi_\pm}{\partial t} \pm c \frac{\partial \phi_\pm}{\partial x} = \left(\frac{g_o - \alpha_o}{1 + (\phi_+ + \phi_-)/\phi_s} - \alpha \right) \phi_\pm \qquad (5)$$

where $\phi_+(\phi_-)$ is the cavity flux propagating in the positive (negative) x direction, ϕ_s is the saturation flux, g_o is the small signal gain, α_o and α are the saturable and nonsaturable absorption coefficients of the medium. It should be noted that α_o and g_o have the same saturation flux. Absorption by F_2, F^-, Kr_2^+ and Ar_2^+ is nonsaturable, while the absorption by Kr_2F^* is saturable

TABLE VII

DOMINANT ABSORBING SPECIES

	Cross Section (cm^2)	Ref.
F_2	1.3×10^{-20}	(58)
F^-	5.6×10^{-18}	(59)
Kr_2F	1.6×10^{-18}	(60)

with the same saturation flux as the lasing transition, since KrF* is the precursor of the Kr_2F^*.[51] Equation (5) may be simplified by integrating over x. The temporal variation of the laser cavity flux is then determined by the following differential equation

$$\frac{d\langle\phi_c\rangle}{dt} = c\left(\frac{g_o - \alpha_o}{1 + \langle\phi_c\rangle/\phi_s} - g_c - \alpha\right)\langle\phi_c\rangle \qquad (6)$$

where $\langle\phi_c\rangle$ is the spatially averaged cavity flux, g_c the cavity loss. In writing Eq. (6) we have assumed that (1) the variations of gain and absorption along the cavity are small[61] and (2) the temporal variation of ϕ_c is small during one round trip in the cavity. The photon round trip time in the cavity was ~ 10 ns, whereas, as will be shown subsequently, the cavity flux varied on a time scale of ~ 50 ns. The numerical solution of Eq. (5) was obtained by following the temporal buildup of laser cavity flux from KrF* spontaneous fluorescence. The initial value of the isotropic KrF* fluorescence was determined from the code describing the formation and quenching kinetics. The predicted shape of the laser pulse was only weakly dependent on the calculated value of initial flux, since the transit time of the flux in the laser cavity was short compared to the time scale of the e-beam current density variations.

3. Experimental Results and Comparison with Model Predictions

The data were obtained using a 1-m e-beam excited laser. A cross section of the cold cathode e-gun ($V_{eb} \simeq 250$ keV, $J_{eb} \simeq 12$ A/cm^2) and the laser chamber are shown in Figure 29.

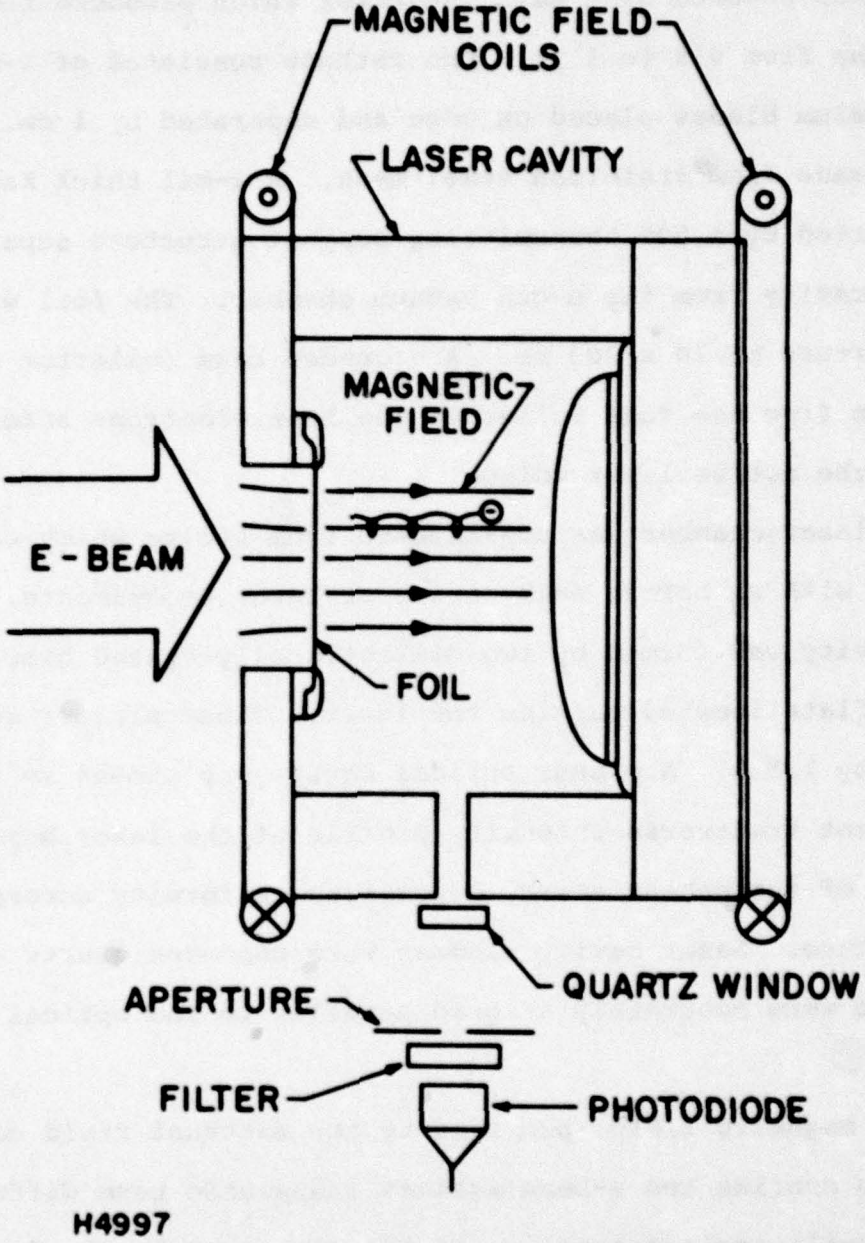

Figure 29 A Cross-Sectional View of the E-Beam and Laser Cavity

The e-gun was powered by a Marx generator which produced beam pulselengths from 0.5 to 1 μs. The cathode consisted of 1-mil thick tantalum blades placed on edge and separated by 1 cm. The anode was made from stainless steel mesh. A 2-mil thick Kapton foil supported by a 90% transmitting support structure separated the laser cavity from the e-gun vacuum chamber. The foil window had an aperture of 10 x 100 cm. A grounded beam collector situated 8.5 cm from the foil collected the beam electrons after they traversed the active laser volume.

The laser chamber was constructed from Lucite which was passivated with F_2 before each series of laser experiments. An optical cavity was formed by two dielectrically-coated quartz (Dynasil) flats located outside the laser. These mirrors were separated by 1.5 m. A planar optical cavity was chosen so that the resultant transverse intensity profile of the laser beam was indicative of the e-beam energy deposition uniformity across the laser aperture. Laser cavity windows were uncoated quartz (Dynasil) flats which were accurately aligned parallel to the optical cavity mirrors.

A dc magnetic field, provided by two external field coils, was used to confine the e-beam against transverse beam diffusion caused by small angle scattering of the electrons by the foil and laser gas mixture. The field was directed parallel to the desired e-beam direction and measured 800 G at the center of the cavity. The e-beam power deposited was calculated from measured voltage and transmitted current traces shown in Figure 30. The beam energy

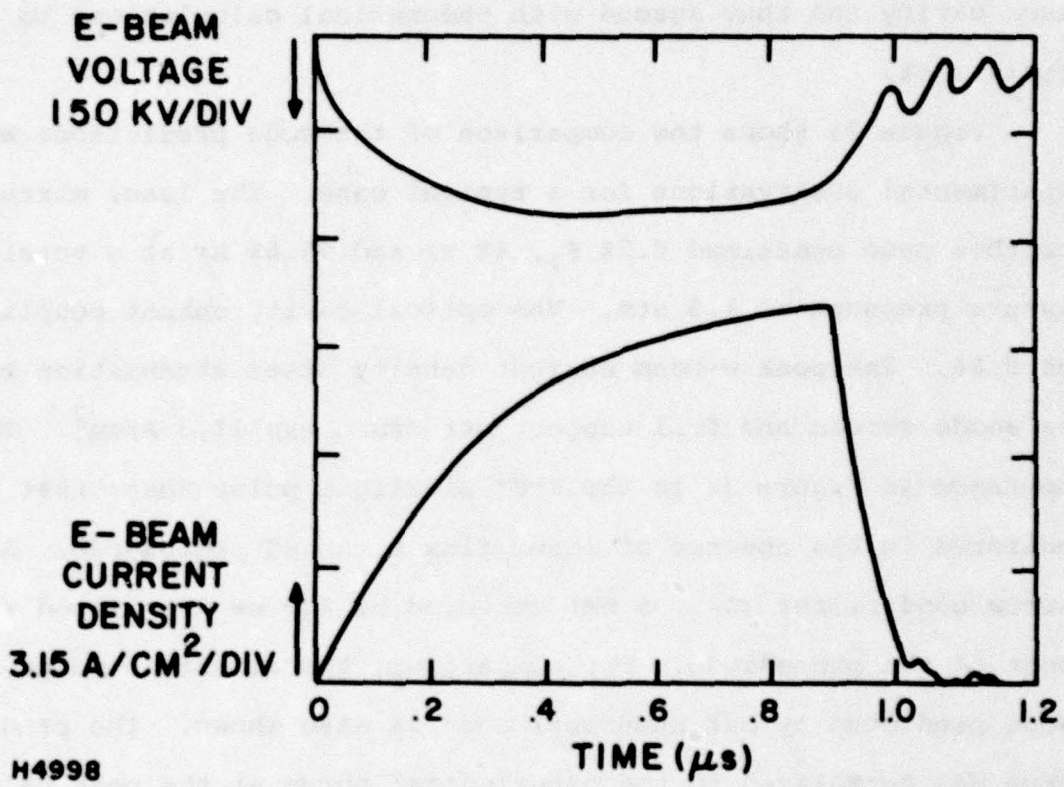

Figure 30 Temporal Shape of the E-Beam Voltage and Current Density

deposited was also calculated from measurements of the cavity overpressure taken after the acoustic disturbance had dissipated. These measurementes were corrected for power radiated from the laser cavity and they agreed with theoretical calculations to within ± 5%.

Figure 31 shows the comparison of the code predictions and experimental observations for a typical case. The laser mixture for this case contained 0.2% F_2, 4% Kr and 95.8% Ar at a total mixture pressure of 1.5 atm. The optical cavity output coupling was 0.66. The peak e-beam current density after attenuation by the anode screen and foil support structure was 11.5 A/cm^2. The top trace in Figure 31 is the KrF* sidelight pulse shape that was monitored in the absence of laser flux by an S5 photodiode. A narrow band filter ($\Delta\lambda$ = 5 nm) centered at 249 nm was placed in front of the photodiode. For comparison, the sidelight pulse shape predicted by our numerical code is also shown. The predicted curve was normalized to the experimental curve at the peak value. The center traces are a comparison of the sidelight under laser conditions.

The bottom traces in Figure 31 show the predicted and experimental laser pulse shapes. Experimentally, the laser energy was measured using a Scientec calorimeter and the pulse shape was monitored by a photodiode. The laser power coupled out was computed by insuring that the integrated power was just the measured output energy. The area of the laser beam was determined from burn pattern measurements so that the output flux could be computed. Notice that

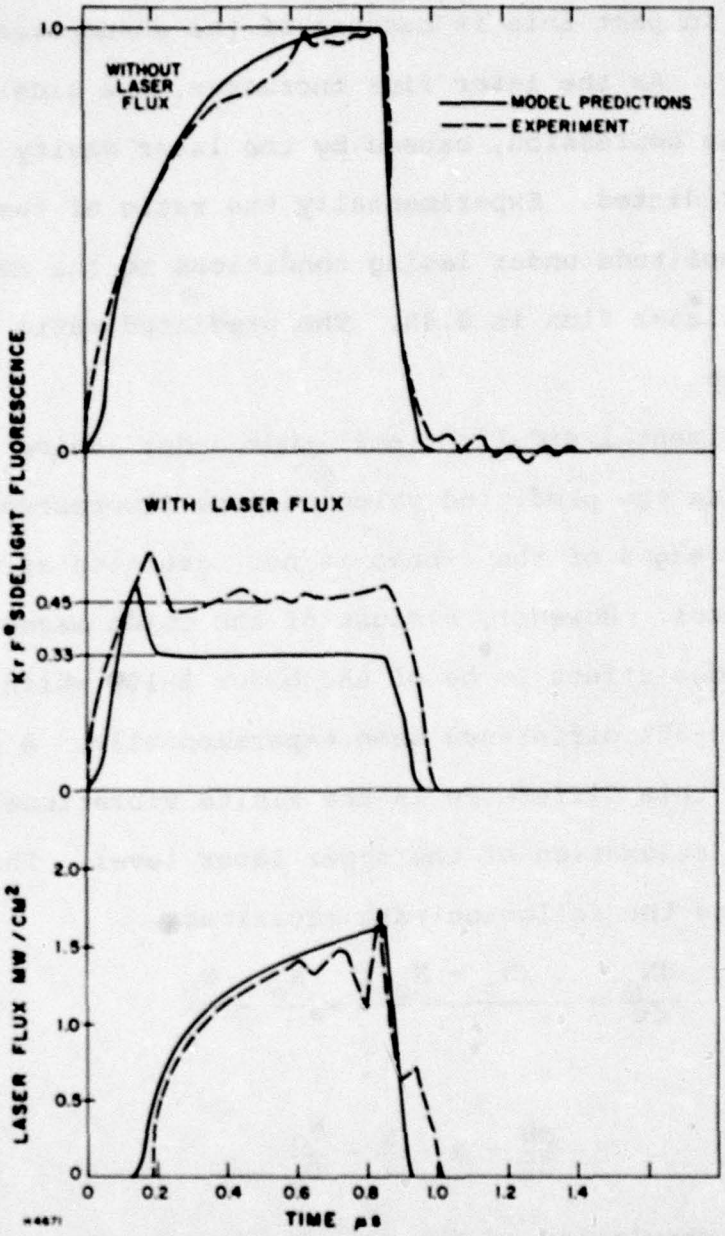

Figure 31 The Top Two Traces are a Comparison Between Numerically Predicted and Measured KrF* Sidelight Pulse Shapes Under Non-Lasing Conditions. The middle two traces are the sidelight pulse shapes under lasing conditions. The bottom traces are a comparison of the predicted and measured laser flux extracted.

the predicted pulse turns on about 40 ns earlier than the experimental pulse. In part this is because of the assumptions made in writing Eq. (6). As the laser flux increases, the sidelight is depressed. This depression, caused by the laser cavity flux, is smaller than predicted. Experimentally the ratio of the sidelight fluorescence amplitude under lasing conditions to the amplitude in the absence of laser flux is 0.45. The predicted ratio is 0.33.

4. Discussion

The experimental sidelight amplitude under lasing is expected to be larger than the predicted value because fluorescence from the upper and lower edges of the e-beam is not saturated as well as that in the center. However, because of the guide magnetic field, we expect the edge effect to be of the order 5-10% which is much less than the 30-35% difference seen experimentally. A possible explanation for this difference is the finite vibrational and perhaps rotational relaxation of the upper laser level. This can be seen by analyzing the following rate equations

$$\frac{dN_o}{dt} = - \frac{(N_o - N_{oe})}{\tau_v} - \frac{N_o}{\tau} - \frac{N_o}{\tau_s} \qquad (7)$$

and

$$\frac{dN}{dt} = R - \frac{N}{\tau} - \frac{N_o}{\tau_s} \qquad (8)$$

where N_o is the population of the zeroth vibrational level; N_{oe} is the equilibrium population of the zeroth level $N_{oe} = \theta_o N$. Where θ_o is the Boltzmann factor and $N = \sum_v N_v$, τ is the lifetime of the upper level, τ is the stimulated lifetime of the upper level, R is the pumping rate and τ_v is the vibrational relaxation rate.

Equations (7) and (8) can be solved under steady-state conditions to give

$$N/N^{o} = \frac{\{1 + (\phi/\phi_s)\ \frac{1}{\beta}\}}{(1 + \phi/\phi_s)} \tag{9}$$

where ϕ_s is the saturation flux defined previously, N^{o} is the upper state population density when $\phi = 0$ and

$$\beta = 1 + \theta_o\ \tau/\tau_v \tag{10}$$

Note that for $\tau_v \to 0$ and $\beta \to \infty$ the depression of the sidelight will be $(1 + \phi/\phi_s)^{-1}$. In our model we have assumed $\tau_v = 0$. To explain the 25-35% difference in the depression we require that

$$\frac{\phi}{\phi_s}\ \frac{1}{\beta} \approx 0.25\text{-}0.35 \text{ or } \beta \approx 8.5 \tag{11}$$

The vibrational spacing of KrF* is estimated[62] to be 310 cm^{-1}. Hence, at room temperature $\theta_o \sim 0.76$. Using the value of β given by Eq. (11) the ratio $\tau/\tau_v \approx 10$. The KrF* lifetime in the laser mixture is ~ 2.9 ns. Hence, we can estimate τ_v the vibrational relaxation time to be ~ 0.29 ns. Assuming that Ar is responsible for the vibrational relaxation, this relaxation time corresponds to a two-body rate constant of $\sim 10^{-10}$ cm^3/s or a three-body rate constant of $\sim 2.7 \times 10^{-30}$ cm^6/s. This finite vibrational relaxation rate will decrease the extraction efficiency by $1/\beta$ (Ref. 6) which is small for this experiment and so we will ignore its effect in the subsequent discussion. However, it should be noted that this decrease in extraction efficiency can be substantial for very high e-beam pumping intensities ($> 10^6$ W/cm^3) where the electron density is high and electron quenching of KrF* can

significantly lower τ. Also the transfer time between the B and C states of KrF may have a similar effect on the extraction efficiency. Again at low pump powers the effect is small, but it could be substantial at the higher pump power.

Figure 32 shows the predicted time dependence of the formation efficiency η_F, fluorescence efficiency η_{FL}, the laser intrinsic efficiency η_{INT}, and the laser extraction efficiency η_{EXT} for the experimental data discussed in Section II.C.3. η_F is the efficiency with which KrF* is created and η_{FL} is the spontaneous power radiated divided by the e-beam power deposited. η_{EXT} is the ratio of the laser flux extracted to the available flux, and η_{INT} is just the product $\eta_{EXT}\eta_F$, which also is equal to the laser output power divided by the e-beam power deposited. Interestingly enough, by the end of the pulse the fluorescence efficiency is 7.5%, while the intrinsic efficiency is almost 9%. The reason that $\eta_{INT} > \eta_{FL}$ is that under lasing conditions the cavity flux is large enough to stimulate the KrF* before it can radiatively decay or be quenched by F_2 and the rare gases. Finally, η_{EXT} and η_{INT} are zero until the laser turns on, which is to be expected.

We have used our code to predict the laser output for a variety of pumping conditions. These predictions are shown in Figure 33 which is a plot of the intrinsic efficiency as a function of e-beam current density. In plotting these curves we have kept $J_{eb}\tau_p$ constant at 7.5×10^{-6} coulombs/cm^2, i.e., the pump pulse energy into the laser mixture was held constant. For this pump energy half the F_2 is burnt by the end of the pulse.

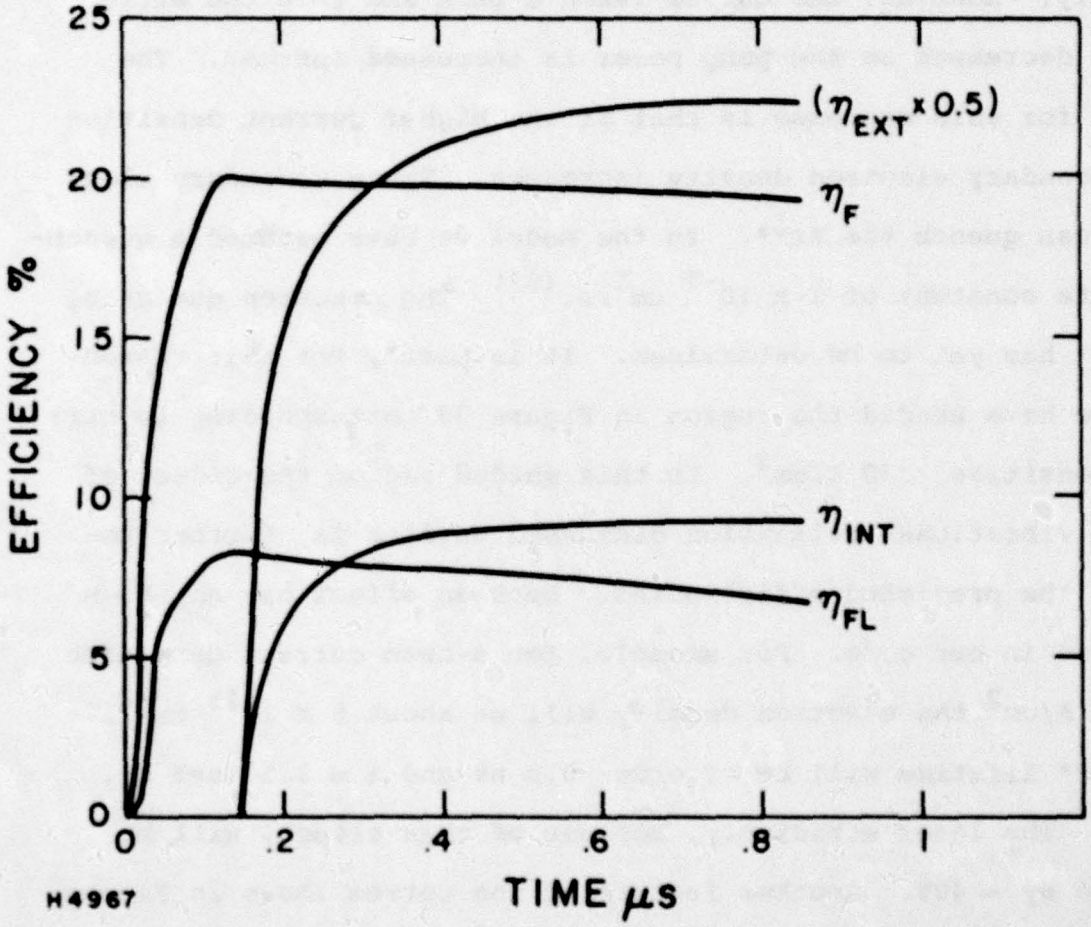

Figure 32 Plots Showing the Predicted Values of η_{EXT}, η_F, η_{INT} and η_{FL}. Note that the curve for η_{EXT} is divided by two.

Notice that for a given laser length of < 2 m the laser efficiency first rises as the e-beam current density increases. This increase is because the absorbing species F^- increases only as the square root of the pump power whereas the gain increases linearly. However, the curves reach a peak and then the efficiency decreases as the pump power is increased further. The reason for this decrease is that at the higher current densities the secondary electron density increases. These secondary electrons can quench the KrF*. In the model we have assumed a quenching rate constant of 2×10^{-7} cm^3/s.[63] The electron quenching of KrF* has yet to be determined. It is partly for this reason that we have shaded the region in Figure 33 corresponding to current densities > 30 A/cm^2. In this shaded region the effect of finite vibrational relaxation discussed earlier may further decrease the predicted efficiencies. Such an effect has not been included in our code. For example, for e-beam current densities of 100 A/cm^2 the electron density will be about 5×10^{15} cm^{-3}. The KrF* lifetime will be of order 0.8 ns and $\beta \approx 2.5$ (see Eq. (10)). The laser efficiency, because of this effect, will be reduced by ~ 40%. Another feature of the curves shown in Figure 33 is that the efficiency for longer laser lengths also decrease as the length increases. This decrease is because the product of the absorption and the laser length is greater than unity.[6]

For the present laser device the highest output energy and the highest intrinsic efficiency were observed at a filling pressure of 1.7 atm (0.2% F_2/4% Kr/95.8% Ar), an average transmitted current

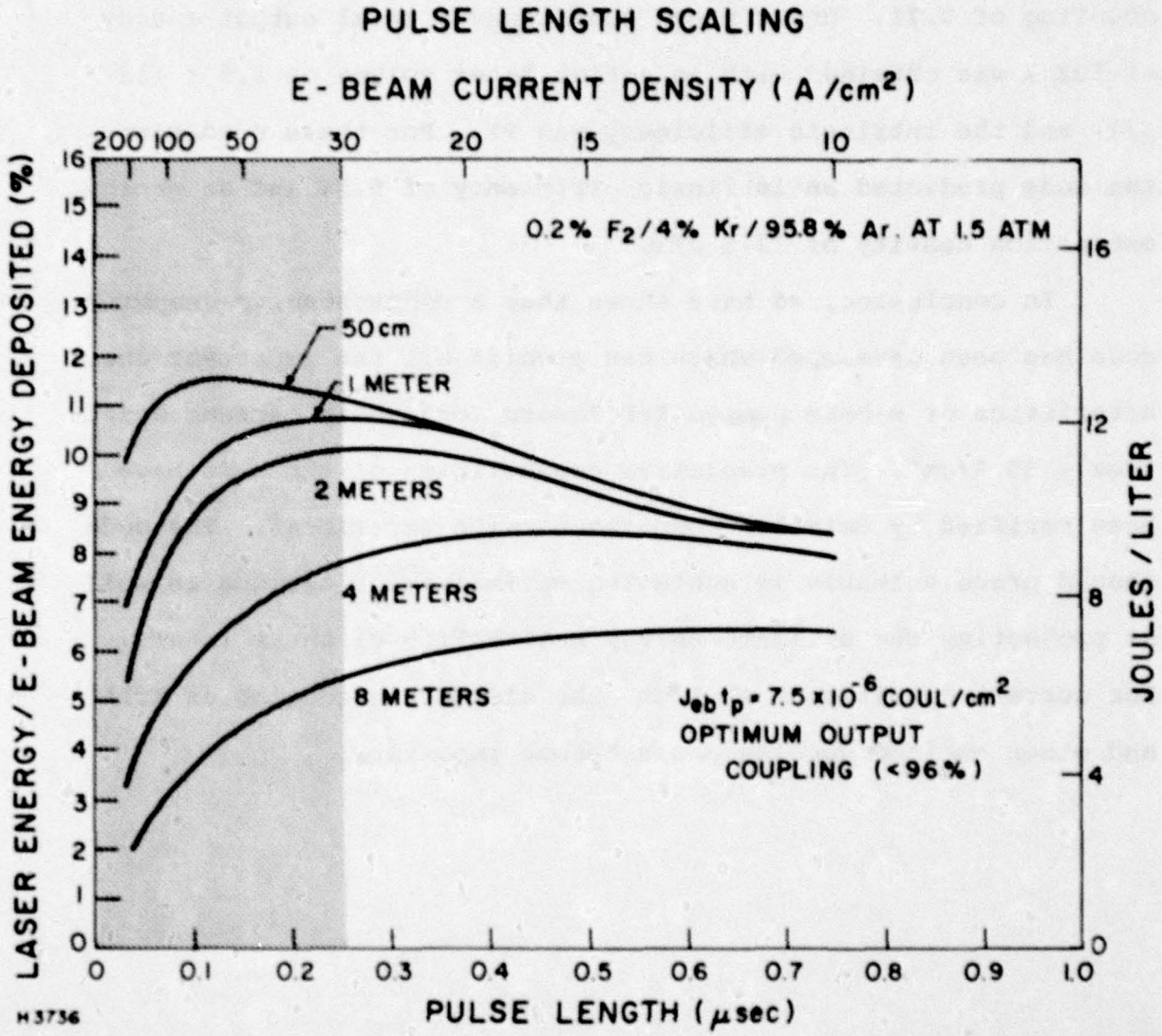

Figure 33 Scaling Map for the KrF* Laser

of 11.5 A/cm^2 (13.5 A/cm^2 peak) and an optical cavity output coupling of 0.71. Under these conditions a total output energy of 102 J was obtained with an active laser volume of 8.5 l (12 J/l) and the intrinsic efficiency was 9%. For these conditions the code predicted an intrinsic efficiency of 9.3% and an energy extraction density of 12.5 J/l.

In conclusion, we have shown that a comprehensive computer code has been developed which can predict all the important characteristics of e-beam pumped KrF lasers for e-beam current densities < 30 A/cm^2. The predictive capabilities of the code have been verified by detailed comparisons with experiment. The code should prove valuable in achieving optimal laser designs as well as projecting the ultimate energy scalability of these lasers. For current densities > 30 A/cm^2 the electron quenching of KrF* and other excited species could become important.

REFERENCES

1. Mangano, J.A. and Jacob, J.H., Appl. Phys. Lett. 27, 495 (1975).

2. Daugherty, J.D., Mangano, J.A. and Jacob, J.H., Appl. Phys. Lett. 28, 581 (1976).

3. Jacob. J.H. and Mangano, J.A., Appl. Phys. Lett. 28, 724 (1976).

4. Hawryluk, A.M., Mangano, J.A. and Jacob, J.H., Appl. Phys. Lett. 31, 164 (1977).

5. Rokni, M., Jacob, J.H. and Mangano, J.A., Appl. Phys. Lett. 32, 622 (1978).

6. Rokni, M. Mangano, J.A., Jacob, J.H. and Hsia, J.C., IEEE J. Quan. Elec. QE-14, 464 (1978).

7. Jacob, J.H., Mangano, J.A., Rokni, M. and Srivastava, B.N., Bull. Am. Phys. Soc. 23, 147 (1978).

8. Srivastava, B.N., Jacob, J.H., Mangano, J.A. and Rokni, M., Appl. Phys. Lett. 32 705 (1978).

9. Trainor, D.W., Rokni, M., Jacob, J.H. and Mangano, J.A., Gaseous Electronics Conf., Paper CA-5. October 1978

10. Srivastava, B.N., Jacob, J.H. and Rokni, M., Interim Technical Report. December 1978

11. Krause, H.F., Johnson, S.A., Datz, S. and Schmidt-Bleek, S.K., Chem. Phys. Lett. 31, 577 (1975).

12. Tam, Wing-Cheung and Wong, S.F., unpublished.

13. Kurepa, M.V. and Belic, D.S., Chem. Phys. Lett. 49, 608 (1977).

14. Spence, D. and Schulz, G.J., J. Chem. Phys. 58, 1800 (1973).

15. Gibson, G.E. and Bayliss, N.S., Phys. Rev., 44, 188 (1933).

16. For a complete discussion on the Boltzmann Equation and a review of past work see Aldo L. Gillandini, "Low Energy Electron Collision in Gases," Wiley, New York, (1972).

17. Christodoulides, A.A., Schumacher, R. and Schindler, R.N., J. Chem. Phys. 79, 1904 (1975).

18. Rockwood, Stephen D., Phys. Rev. A 8, 2343 (1973).

19. Smith, A.L. and Kobrinsky, P.C., J. Mol. Spec. 69, 1 (1978); Tellinghuisen, P.C., Tellinghuisen, J., Coxon, J.A., Velazco, J.E. and Setser, D.W., J. Chem. Phys. 68, 5187 (1978).

20. Krauss, M., NBS, private communication.

21. Kolts, H.J. and Setser, D.W., J. Phys. Chem. 82, 1766 (1978), see also Setser, D.W., Third Quarterly Progress Report, DoE, July (1978).

22. Kligler, D., Nakano, H.H., Huestis, D.L., Bischel, N.K., Hill, R.M. and Rhodes, C.K., Appl. Phys. Lett. 33, 39 (1978).

23. Julienne and Krauss, unpublished.

24. Emission from the triatomic ArXeF* has been previously investigated by Hunter, R.O., J. Oldenettel, Howton, C. and McCusker, M.V., J. Appl. Phys. 49, 549 (1978).

25. Hsia, J.C., Mangano, J.A., Jacob, J.H. and Rokni, M., Appl. Phys. Lett. 34, 208 (1979).

26. Finn, T.G., Palumbo, J.L. and Champagne, L.F., Appl. Phys. Lett. 34, 52 (1979).

27. Hawrylwk, A.M., Mangano, J.A. and Jacob, J.H., Appl. Phys. Lett. 31, 164 (1977).

28. Rokni, M., Jacob, J.H. and Mangano, J.A., Appl. Phys. Lett. 32, 622 (1978).

29. Hsia, J.C., Mangano, J.A., Jacob, J.H. and Rokni, M. Appl. Phys. Lett. 34, 208 (1979).

30. Rokni, M. Jacob, J.H., MAngano, J.A. and Brochu, R. Appl. Phys. Lett. 30, 458 (1977).

31. Rokni, M., Jacob, J.H., Mangano, J.A. and Brochu, R., Appl. Phys. Lett. 31, 79 (1977).

32. Fisher, C.H. and Center, R.E., J. Chem. Phys. 69, 2011 (1978).

33. Eden, J.G. and Searles, S.K., Appl. Phys. Lett. 30, 287 (1977).

34. Ewing, J.J., Seventh Winter Colloquium on Quantum Electronics, (Park City, Utah, 1977).

35. Burnham, R. and Harris, N.W., J. Chem. Phys. 66, 2742 (1977).

36. Burnham, R. and Searles, S.K., Paper AA-3, 30th Annual Gaseous Electronics Conference, Palo Alto, CA (Oct. 1977); J. Chem. Phys. 68, 2850 (1978).

37. Eden, J.G. and Waynant, R.W., Paper AA-5, 30th Anneual Gaseous Electronics Conference, Palo Alto, CA. October 1977.

38. Brashears, H.C., Setser, D.W. and DesMarteau, D., Chem. Phys. Lett. 48, 84 (1977).

39. Shui, V. and Duzy, C., private communication, (1978).

40. Schneider, B. and Brau, C., Conference on Visible Lasers, Gif-zur-Yvette, France (1978).

41. Trainor, D.W. and Jacob, J.H., Appl. Phys. Lett. (submitted 1979).

42. Rokni, M., Jacob, J.H. and Mangano, J.A., Appl. Phys. Lett. 34, 187 (1979).

43. Brashears, H.C. and Setser, D.W., Appl. Phys. Lett. 33, 821 (1978).

44. Tellinghuisen, J., Tiscone, G.C., Hoffman, J.M. and Hays, A.K., J. Chem. Phys. 64, 4796 (1976).

45. Shui, V., AERL, private communication; Heustis, D., Lorentz, D., Hill, R.M. and McCusker, M., SRI Int. Report #MP78-07, May 1978.

46. Fulghum, S.F., Herman, I.P., Feld, M.S. and Javan, J. Appl. Phys. Lett. 33, 926 (1978).

47. For typical laser mixtures, the upper level lifetime is ~ 5 ns. If the rotational relaxation of XeF is similar to CO_2, then τ_{rot} ~ 170 ps/atm (see Ref 48). Since the experiments discussed are performed at 3 atm, then τ_{rot} ~ 60 ps and our assumption is valid. However, for heated XeF the dissociative lifetime of the lower level is reduced and this assumption might not hold. Finally, the experiment cited in Ref. 49 has shown that rotational relaxation is rapid compared to the upper level lifetime.

48. See for example: Feldman, B., Opt. Comm., 14, 13 (1975) and IEEE JQE, QE-9, 231 (1973) and Cheo, P.K. and Abrams, R.L., Appl. Phys. Lett. 14, 47 (1969).

49. Goldhar, J., Dicke, J., Bradley, L.P. and Pleasance, L.D., Appl. Phys. Lett. 31, 677 (1977).

50. Shui, V. and Duzy, C., (unpublished).

51. Rokni, M., Jacob, J.H. and Mangano, J.A., Phys. Rev. A16, 2216 (1977).

52. Velazco, J.E., Kolts, J.H. and Setser, D.W., J. Chem. Phys. 65, 3468 (1976).

53. Jesse, W.P. and Sadauskis, J., Phys. Rev. 90, 1120L (1953).

54. Chen, Hao-Lin, Center, R.E., Trainor, D.W. and Fyfe, W.I., J. Appl. Phys. 48, 2297 (1977).

55. Jacob, J.H., Rokni, M. Mangano, J.A. and Brochu, R., Appl. Phys. Lett. 32, 109 (1978).

56. Flannery, M.R. and Yang, T.P., Appl. Phys. Lett. 32, 327 (1978); See also Appl. Phys. Lett. 32, 356 (1978).

57. Other scientists have investigated the quenching of KrF* and obtained rates similar to those used in this article. See, for example Eden, J.G., Wayant, R.W., Searles, S.K., and Burnham, R., Appl. Phys. Lett. 32, 733 (1978); Quigley, G.P. and Hughes, W.M., Appl. Phys. Lett. 32, 627 (1978).

58. Steunenberg, R.K. and Vogel, R.C., J. Amer. Chem. Soc. 78, 901, (1956).

59. Mandl, A., Phys. Rev. A3, 251 (1970).

60. Stevens, W.J., Gardner, M. and Karo, A., J. Chem. Phys. 67, 2860 (1977); Wadt, W.R., Cartwright, D.C. and Cohen, J.S., Appl. Phys. Lett. 31, 672 (1977).

61. The condition on the small variation of gain on absorption with x may be written explicitly as

$$\left| \left\langle \frac{\phi_c/\phi_s}{1 + \phi_c/\phi_s} \right\rangle - \frac{\langle \phi_c/\phi_s \rangle}{1 + \langle \phi_c/\phi_s \rangle} \right| \Bigg/ \left\langle \frac{\phi_c/\phi_s}{1 + \phi_c/\phi_s} \right\rangle \ll 1$$

where $\langle F \rangle = \frac{1}{2} \int F(x)dx$. For the example discussed subsequently this ratio < 0.1.

62. Tellinghuisen, J., Hays, A.K., Hoffman, J.M. and Tiscone, G.C., J. Chem. Phys. 65, 4473 (1976).

63. Trainor, D.W., Rokni, M. and JAcob, J.H., 31st Gaseous Electronic Conference, Buffalo, Oct. (1978). In our model we have also assumed that the precursor for KrF* such as ArF* can be quenched by electrons. The rate constant used for this process is 2×10^{-7} cm^3/s.

DISTRIBUTION LIST

Office of Naval Research, Department of the Navy, Arlington, VA 22217 - Attn: Physics Program (3 copies)

Naval Research Laboratory, Department of the Navy, Washington, D.C. 20375 - Attn: Technical Library (1 copy)

Office of the Director of Defense, Research and Engineering, Information Office Library Branch, The Pentagon, Washington, D.C. 20301 (1 copy)

U.S. Army Research Office, Box CM, Duke Station, Durham, N.C. 27706 (1 copy)

Defense Documentation Center, Cameron Station, Alexandria, VA 22314 (12 copies)

Defender Information Analysis Center, Battelle Memorial Institute, 505 King Avenue, Columbus, OH 43201 (1 copy)

Commanding Officer, Office of Naval Research Branch Office, 536 South Clark Street, Chicago, IL 60615 (1 copy)

New York Area Office, Office of Naval Research, 715 Broadway (5th floor), New York, NY 10003 - Attn: Dr. Irving Rowe (1 copy)

Air Force Office of Scientific Research, Department of the Air Force, Washington, DC 22209 (1 copy)

Office of Naval Research Branch Office, 1030 East Green Street, Pasadena, CA 91106 - Attn: Dr. Robert Behringer (1 copy)

Defense Advanced Research Projects Agency, 1400 Wilson Blvd., Arlington, VA 22209 - Attn: Strategic Technology Office (1 copy)

Office Director of Defense, Research & Engineering, The Pentagon, Washington, DC 20301 - Attn: Asst. Dir.(Space and Advanced Systems) (1 copy)

Office of the Asst Secretary of Defense, System Analysis (Strategic Programs), Washington, DC 20301 (1 copy)

U.S. Arms Control and Disarmament Agency, Dept. of State Bldg., Rm. 4931, Washington, DC 20451 - Attn: Dr. Charles Henkin (1 copy)

Energy Research Development Agency, Division of Military Applications, Washington, DC 20545 (1 copy)

National Aeronautics and Space Administration, Lewis Research Center, Cleveland, OH 44135 - Attn: Dr. John W. Dunning, Jr (Aerospace Res. Engineer) (1 copy)

National Aeronautics & Space Administration, Code RR, FOB 10B, 600 Independence Ave., SW, Washington, DC 20546 (1 copy)

National Aeronautics and Space Administration, Ames Research Center, Moffett Field, CA 94035 - Attn: Dr. Kenneth W. Billman (1 copy)

Department of the Army, Office of the Chief of RD&A, Washington, DC 20310, Attn: DARD-DD (1 copy)
DAMA-WSM-T (1 copy)

Department of the Army, Office of the Deputy Chief of Staff for Operations & Plans, Washington, DC 20310 - Attn: DAMO-RQD (1 copy)

Ballistic Missile Defense Program Office (BMDPO), The Commonwealth Building, 1300 Wilson Blvd., Arlington, VA 22209 - Attn: Mr. Albert J. Baat, Jr. (1 copy)

U.S. Army Missile Command, Research and Development Division, Redstone Arsenal, ALA 35809 - Attn: Army High Energy Laser Programs (2 copies)

Commander, Rock Island Arsenal, Rock Island, IL 61201 - Attn: SARRI-LR, Mr. J.W. McGarvey (1 copy)

Commanding Officer, U.S. Army Mobility Equipment R&D Center, Ft. Belvoir, VA 22060 - Attn: SMEFB-MW (1 copy)

Commander, U.S. Army Armament Command, Rock Island, IL 61201 - Attn: AMSAR-RDT (1 copy)

Director, Ballistic Missile Defense Advanced Technology Center, P.O. Box 1500, Huntsville, AL 35807 - Attn: ATC-O (1 copy)
ACT-T (1 copy)

Commander, U.S. Army Material Command, Alexandria, VA 22304 - Attn: Mr. Paul Chernoff (AMCRD-T) (1 copy)

Commanding General, U.S. Army Munitions Command, Dover, NH 17801 - Attn: Mr. Gilbert F. Cheanov (AMSMU-R) (1 copy)

Director, U.S. Army Ballistics Res. Lab, Aberdeen Proving Ground, MD 21005 - Attn: Dr. Robert Eichenberger (1 copy)

Commandant, U.S. Army, Air Defense School, Ft. Bliss, TX 79916 - Attn: Air Defense Agency (1 copy)
ATSA-CTD-MS (1 copy)

Commanding General, U.S. Army Combat Dev. Command, Ft. Belvoir, VA 22060 - Attn: Director of Material, Missile Div. (1 copy)

Commander, U.S. Army Training & Doctrine Command, Ft. Monroe, VA 23651 - Attn: ATCD-CF (1 copy)

Commander, U.S. Army Frankford Arsenal, Philadelphia, PA 19137 - Attn: Mr. M. Ehrick SARFA-FCD, Bldg. 201-3 (1 copy)

Commander, U.S. Army Electronics Command, Ft. Monmouth, NJ 07703 - Attn: AMSEL-CT-L, Dr. R.G. Buser (1 copy)

Commander, U.S. Army Combine Arms Combat Developments Activity, Ft. Leavenworth, KS 66027 (1 copy)

National Security Agency, Ft. Geo. G. Meade, MD 20755 - Attn: R.C. Foss A763 (1 copy)

Deputy Commandant for Combat & Training Developments, U.S. Army Ordnance Center & School, Aberdeen Proving Ground, MD 21005 - Attn: ATSL-CTD-MSR (1 copy)

Commanding Officer, USACDC CBR Agency, Ft. McClellan, AL 36201 - Attn: CDCCBR-MR (Mr. F.D. Poer) (1 copy)

Department of the Navy, Office of the Chief of Naval Operations, The Pentagon SC739, Washington, DC 20350 - Attn: (OP 982F3) (1 copy)

Office of Naval Research Branch Office, 495 Summer Street, Boston, MA 02210 - Attn: Dr. Fred Quelle (1 copy)

Department of the Navy, Deputy Chief of Navy Material (Dev.), Washington, DC 20360 - Attn: Mr. R. Gaylord (MAT 032B) (1 copy)

Naval Missile Center, Point Mugu, CA 93042 - Attn: Gary Gibbs (Code 5352) (1 copy)

Naval Research Laboratory, Washington, DC 20375 - Attn: (Code 5503-EOTPO) (1 copy)
Dr. F. Livingston - Code 5560 (1 copy)
Dr. A.I. Schindler - Code 6000 (1 copy)
Dr. H. Shenkey - Code 5504 (1 copy)
Mr. D.J. McLaughlin - Code 5560 (1 copy)
Dr. John L. Walsh - Code 5503 (1 copy)

High Energy Laser Project Office, Department of the Navy, Naval Sea Systems Command, Washington, DC 20360 - Attn: CAPT A. Skolnick, USN (PM 22) (1 copy)

Superintendent, Naval Postgraduate School, Monterey, CA 93940 - Attn: Library (Code 2124) (1 copy)

Navy Radiation Technology, Air Force Weapons Lab (NLO), Kirtland AFB, NM 87117 (1 copy)

Naval Surface Weapons Center, White Oak, Silver Spring, MD 20910 - Attn: Dr. Leon H. Schindel (Code 310) (1 copy)
Dr. E. Leroy Harris (Code 313) (1 copy)
Mr. K. Enkenhaus (Code 034) (1 copy)
Mr. J. Wise (Code 047) (1 copy)
Technical Library (1 copy)

U.S. Naval Weapons Center, China Lake, CA 93555 - Attn: Technical Library (1 copy)

HQ AFSC/XRLW, Andrews AFB, Washington, DC 20331 - Attn: MAJ J.M. Walton (1 copy)

HQ AFSC (DLCAW), Andrews AFB, Washington, DC 20301 - Attn: MAJ H. Axelrod (1 copy)

Air Force Weapons Laboratory, Kirtland AFB, NM 87117 - Attn: LR (1 copy)
AL (1 copy)

HQ SAMSO (XRTD), P.O. Box 92960, Worldway Postal Center, Los Angeles, CA 90009 - Attn: LT Dorian DeMalo (XRTD) (1 copy)

AF Avionics Lab (TEO), Wright Patterson AFB, OH 45433 - Attn: Mr. K. Hutchinson (1 copy)

Dept of the Air Force, Air Force Materials Lab. (AFSC), Wright Patterson AFB, OH 45433 - Attn: MAJ Paul Ejder (LPS) (1 copy)
Laser Window Group

HQ Aeronautical Systems Div., Wright Patterson AFB, OH 45433 - Attn: XRF - Mr. Clifford Fawcett (1 copy)

Rome Air Development Command, Griffiss AFB, Rome, NY 13440 - Attn: Mr. R. Urtz (OCSE) (1 copy)

HQ Electronics Systems Div. (ESL), L.G. Hanscom Field, Bedford, MA 01730 - Attn: Mr. Alfred E. Anderson (XRT) (1 copy)
Technical Library (1 copy)

Air Force Rocket Propulsion Lab., Edwards AFB, CA 93523 - Attn: B.E. Bornhorst, (LKCG) (1 copy)

Air Force Aero Propulsion Lab., Wright Patterson AFB, OH 45433 - Attn: COL Walter Mow (CC) (1 copy)

Dept. of the Air Force, Foreign Technology Division, Wright Patterson AFB, OH 45433 - Attn: PDTN (1 copy)

Commandant of the Marine Corps, Scientific Advisor (Code RD-1), Washington, DC 20380 (1 copy)

Aerospace Research Labs., (AF), Wright Patterson AFB, OH 45433 - Attn: LT COL Max Duggins (1 copy)

Defense Intelligence Agency, Washington, DC 20301 - Attn: Mr. Seymour Berler (DT1B) (1 copy)

Central Intelligence Agency, Washington, DC 20505 - Attn: Mr. Julian C. Nall (1 copy)

Aireserch Manuf. Co., 9851-9951 Sepulveda Blvd., Los Angeles, CA 90009 - Attn: Mr. A. Colin Stancliffe (1 copy)

Atlantic Research Corp., Shirley Highway at Edsall Road, Alexandria, VA 22314 - Attn: Mr. Robert Naismith (1 copy)

Avco Everett Research Lab., 2385 Revere Beach Parkway, Everett, MA 02149 - Attn: Dr. George Sutton (1 copy)
Dr. Jack Daugherty (1 copy)

Battelle Columbus Laboratories, 505 King Avenue, Columbus, OH 43201 - Attn: Mr. Fred Tietzel (STPIAC) (1 copy)

Bell Aerospace Co., Buffalo, NY 14240 - Attn: Dr. Wayne C. Solomon (1 copy)

Boeing Company, P.O. Box 3999, Seattle, WA 98124 - Attn: Mr. M.L. Gamble (2-,460, MS 8C-88) (1 copy)

Electro-Optical Systems, 300 N. Halstead, Pasadena, CA 91107 - Attn: Dr. Andrew Jensen (1 copy)

General Electric Co., Space Division, P.O. Box 8555, Philadelphia, PA 19101 - Attn: Dr. R.R. Siglemonti (1 copy)

General Electric Co., 100 Plastics Avenue, Pittsfield, MA 01201 - Attn: Mr. D.G. Harrington (Rm 1044) (1 copy)

General Research Corp., P.O. Box 3587, Santa Barbara, CA 93105 - Attn: Dr. R. Holbrook (1 copy)

General Research Corp., 1501 Wilson Blvd., Suite 700, Arlington, VA 22209 - Attn: Dr. Giles F. Crimi (1 copy)

Hercules, Inc., Industrial System Dept., Wilmington, DE 19899 - Attn: Dr. R.S. Voris (1 copy)

Hercules, Inc., P.O. Box 210, Cumberland, MD 21502 - Attn: Dr. Ralph R. Preckel (1 copy)

Hughes Research Labs, 3011 Malibu Canyon Road, Malibu, CA 90265 - Attn: Dr. D. Forster (1 copy)

Hughes Aircraft Co., Aerospace Group - Systems Division, Canoga Park, CA 91304 - Attn: Dr. Jack A. Alcalay (1 copy)

Hughes Aircraft Co., Centinela and Teale Streets, Bldg. 6, MS E-125, Culver City, CA 90230 - Attn: Dr. William Yates (1 copy)

Institute for Defense Analyses, 400 Army-Navy Drive, Arlington, VA 22202 - Attn: Dr. Alvin Schnitzler (1 copy)

Lawrence Livermore Laboratory, P.O. Box 808, Livermore, CA 94550 - Attn: Dr. R.E. Kidder (1 copy)
Dr. E. Teller (1 copy)
Dr. Joe Fleck (1 copy)

Los Alamos Scientific Laboratory, P.O. Box 1663, Los Alamos, NM 87544 - Attn: Dr. Keith Boyer (1 copy)

Lockheed Palo Alto Res. Lab., 3251 Hanover St., Palo Alto, CA 94303 - Attn: L.R. Lunsford, Orgn. 52-24, Bldg. 201 (1 copy)

Mathematical Sciences Northwest, Inc., P.O. Box 1887, Bellevue, WN 98009 - Attn: Dr. Abraham Hertzberg (1 copy)

Martin Marietta Corp., P.O. Box 179, Mail Station 0471, Denver, CO 80201 - Attn: Mr. Stewart Chapin (1 copy)

Massachusetts Institute of Technology, Lincoln Laboratory, P.O. Box 73, Lexington, MA 02173 - Attn: Dr. S. Edelberg (1 copy)
Dr. L.C. Marquet (1 copy)

McDonnell Douglas Astronautics Co., 5301 Bolsa Avenue, Huntington Beach, CA 92647 - Attn: Mr. P.L. Klevatt (1 copy)
Dept. A3-830-BBFO, M/S 9

McDonnell Douglas Research Labs, Dept. 220, Box 516, St. Louis, MO 63166 - Attn: Dr. D.P. Ames (1 copy)

MITRE Corp., P.O. Box 208, Bedford, MA 01730 - Attn: Mr. A.C. Cron (1 copy)

Northrop Corp., 3401 West Broadway, Hawthorne, CA 90250 - Attn: Dr. Gerard Hasserjian (1 copy)
Laser Systems Dept.

Physical Sciences, Inc., 19 Lakeside Office Park, Wakefield, Ma 01880 - Attn: Dr. Anthony N. Pirri (1 copy)

RAND Corp., 1700 Main Street, Santa Monica, CA 90406 - Attn: Dr. C.R. Culp/Mr. G.A. Carter (1 copy)

Raytheon Co., 28 Seyon Street, Waltham, MA 02154 - Attn: Dr. F.A. Horrigan (Res. Div.) (1 copy)

Raytheon Co., Boston Post Road, Sudbury, MA 01776 - Attn: Dr. C. Sonnenschien (Equip. Div.) (1 copy)

Raytheon Co., Bedford Labs, Missile Systems Div., Bedford, MA 01730 - Attn: Dr. H.A. Mehlhorn (1 copy)

Riverside Research Institute, 80 West End Street, New York, NY 10023 - Attn: Dr. L.H. O'Neill (1 copy)
Dr. John Bose (1 copy)
(HPEGL Library) (1 copy)

R&D Associates, Inc., P.O. Box 3580, Santa Monica, CA 90403 - Attn: Dr. R.E. LeLevier (1 copy)

Rockwell International Corporation, Rocketdyne Division, Albuquerque District Office, 3636 Menaul Blvd., NE, Suite 211, Albuquerque, NM 87110
Attn: C.K. Kraus, Mgr. (1 copy)

SANDIA Corp., P.O. Box 5800, Albuquerque, NM 87115 - Attn: Dr. Al Narath (1 copy)

Stanford Research Institute, Menlo Park, CA 94025 - Attn: Dr. F.T. Smith (1 copy)

Science Applications, Inc., 1911 N. Ft. Meyer Drive, Arlington, VA 22209 - Attn: L. Peckam (1 copy)

Science Application, Inc., P.O. Box 328, Ann Arbor, MI 48103 - Attn: R.E. Meredith (1 copy)

Science Applications, Inc., 6 Preston Court, Bedford, MA 01703 - Attn: R. Greenberg (1 copy)

Science Applications, Inc., P.O. Box 2351, La Jolla, CA 92037 - Attn: Dr. John Aamus (1 copy)

Systems, Science and Software, P.O. Box 1620, La Jolla, CA 92037 - Attn: Alan F. Klein (1 copy)

Systems, Consultants, Inc., 1050 31st Street, NW, Washington, DC 20007 - Attn: Dr. R.B. Keller (1 copy)

Thiokol Chemical Corp., WASATCH Division, P.O. Box 524, Brigham City, UT 84302 - Attn: Mr. J.E. Hansen (1 copy)

TRW Systems Group, One Space Park, Bldg. R-1, Rm. 1050, Redondo Beach, CA 90278 - Attn: Norman Campbell (1 copy)

United Technologies Research Center, 400 Main Street, East Hartford, CT 06108 - Attn: Mr. G.H. McLafferty (3 copies)

United Technologies Research Center, Pratt and Whitney Acft. Div., Florida R&D Center, West Palm Beach, FL 33402 - Attn: Dr. R.A. Schmidtke (1 copy)
Mr. Ed Pinaley (1 copy)

VARIAN Associates, EIMAC Division, 301 Industrial Way, San Carlos, CA 94070 - Attn: Mr. Jack Quinn (1 copy)

DISTRIBUTION LIST (Continued)

Vought Systems Division, LTV Aerospace Corp., P.O. Box 5907, Dallas, TX 75222 - Attn: Mr. F.G. Simpson, MS 254142 (1 copy)
Westinghouse Electric Corp., Defense and Space Center, Balt-Wash. International Airport - Box 746, Baltimore, MD 21203 - Attn: Mr. W.F. List (1 copy)
Westinghouse Research Labs, Beulah Road, Churchill Boro, Pittsburgh, PA 15235 - Attn: Dr. E.P. Riedel (1 copy)
United Technologies Research Center, East Hartford, CT 06108 - Attn: A.J. deMaria (1 copy)
Airborne Instruments Laboratory, Walt Whitorian Road, Melville, NY 11746 - Attn: F. Pace (1 copy)
General Electric R&D Center, Schenectady, NY 12305 - Attn: Dr. Donald White (1 copy)
Cleveland State University, Cleveland, OH 44115 - Attn: Dean Jack Soules (1 copy)
EXXON Research and Engineering Co., P.O. Box 8, Linden, NJ 07036 - Attn: D. Grafstein (1 copy)
University of Maryland, Department of Physics and Astronomy, College Park, MD 20742 - Attn: D. Currie (1 copy)
Sylvania Electric Products, Inc., 100 Fergeson Drive, Mountain View, CA 94040 - Attn: L.M. Osterink (1 copy)
North American Rockwell Corp., Autonetics Division, 3370 Miraloma Avenue, Anaheim, CA 92803 - Attn: K. Gudmundsen (1 copy)
Massachusetts Institute of Technology, 77 Massachusetts Avenue, Cambridge, MA 02138 - Attn: Prof. A. Javan (1 copy)
Lockheed Missile & Space Co., Palo Alto Research Laboratories, Palo Alto, CA 94304 - Attn: Dr. R.C. Ohlman (1 copy)
H.C Laboratories, Inc., 114 Commercial Street, Sunnyvale, CA 94086 - Attn: L. Noble (1 copy)
University of Texas at Dallas, P.O. Box 30365, Dallas, TX 75230 - Attn: Prof. Carl B. Collins (1 copy)
Polytechnic Institute of New York, Rt. 110, Farmingdale, NY 11735 - Attn: Dr. William T. Walter (1 copy)